Search for standard model Higgs boson production in association with a W boson using a matrix element technique at CDF in $p\bar{p}$ collisions at $\sqrt{s} = 1.96$ TeV

T. Aaltonen,[21] B. Álvarez González,[9,aa] S. Amerio,[40a] D. Amidei,[32] A. Anastassov,[15,y] A. Annovi,[17] J. Antos,[12] G. Apollinari,[15] J. A. Appel,[15] T. Arisawa,[54] A. Artikov,[13] J. Asaadi,[49] W. Ashmanskas,[15] B. Auerbach,[57] A. Aurisano,[49] F. Azfar,[39] W. Badgett,[15] T. Bae,[25] A. Barbaro-Galtieri,[26] V. E. Barnes,[44] B. A. Barnett,[23] P. Barria,[42c,42a] P. Bartos,[12] M. Bauce,[40b,40a] F. Bedeschi,[42a] S. Behari,[23] G. Bellettini,[42b,42a] J. Bellinger,[56] D. Benjamin,[14] A. Beretvas,[15] A. Bhatti,[46] D. Bisello,[40b,40a] I. Bizjak,[28] K. R. Bland,[5] B. Blumenfeld,[23] A. Bocci,[14] A. Bodek,[45] D. Bortoletto,[44] J. Boudreau,[43] A. Boveia,[11] L. Brigliadori,[6b,6a] C. Bromberg,[33] E. Brucken,[21] J. Budagov,[13] H. S. Budd,[45] K. Burkett,[15] G. Busetto,[40b,40a] P. Bussey,[19] A. Buzatu,[31] A. Calamba,[10] C. Calancha,[29] S. Camarda,[4] M. Campanelli,[28] M. Campbell,[32] F. Canelli,[11,15] B. Carls,[22] D. Carlsmith,[56] R. Carosi,[42a] S. Carrillo,[16,n] S. Carron,[15] B. Casal,[9,l] M. Casarsa,[50a] A. Castro,[6b,6a] P. Catastini,[20] D. Cauz,[50a] V. Cavaliere,[22] M. Cavalli-Sforza,[4] A. Cerri,[26,g] L. Cerrito,[28,t] Y. C. Chen,[1] M. Chertok,[7] G. Chiarelli,[42a] G. Chlachidze,[15] F. Chlebana,[15] K. Cho,[25] D. Chokheli,[13] W. H. Chung,[56] Y. S. Chung,[45] C. I. Ciobanu,[58] M. A. Ciocci,[42c,42a] A. Clark,[18] C. Clarke,[55] G. Compostella,[40b,40a] M. E. Convery,[15] J. Conway,[7] M. Corbo,[15] M. Cordelli,[17] C. A. Cox,[7] D. J. Cox,[7] F. Crescioli,[42b,42a] J. Cuevas,[9,aa] R. Culbertson,[15] D. Dagenhart,[15] N. d'Ascenzo,[15,x] M. Datta,[15] P. de Barbaro,[45] M. Dell'Orso,[42b,42a] L. Demortier,[46] M. Deninno,[6a] F. Devoto,[21] M. d'Errico,[40b,40a] A. Di Canto,[42b,42a] B. Di Ruzza,[15] J. R. Dittmann,[5] M. D'Onofrio,[27] S. Donati,[42b,42a] P. Dong,[15] M. Dorigo,[50a] T. Dorigo,[40a] K. Ebina,[54] A. Elagin,[49] A. Eppig,[32] R. Erbacher,[7] S. Errede,[22] N. Ershaidat,[15,ee] R. Eusebi,[49] S. Farrington,[39] M. Feindt,[24] J. P. Fernandez,[29] R. Field,[16] G. Flanagan,[15,v] R. Forrest,[7] M. J. Frank,[5] M. Franklin,[20] J. C. Freeman,[15] Y. Funakoshi,[54] I. Furic,[16] M. Gallinaro,[46] J. E. Garcia,[18] A. F. Garfinkel,[44] P. Garosi,[42c,42a] H. Gerberich,[22] E. Gerchtein,[15] S. Giagu,[47a] V. Giakoumopoulou,[3] P. Giannetti,[42a] K. Gibson,[43] C. M. Ginsburg,[15] N. Giokaris,[3] P. Giromini,[17] G. Giurgiu,[23] V. Glagolev,[13] D. Glenzinski,[15] M. Gold,[35] D. Goldin,[49] N. Goldschmidt,[16] A. Golossanov,[15] G. Gomez,[9] G. Gomez-Ceballos,[30] M. Goncharov,[30] O. González,[29] I. Gorelov,[35] A. T. Goshaw,[14] K. Goulianos,[46] S. Grinstein,[4] C. Grosso-Pilcher,[11] R. C. Group,[53,15] J. Guimaraes da Costa,[20] S. R. Hahn,[15] E. Halkiadakis,[48] A. Hamaguchi,[38] J. Y. Han,[45] F. Happacher,[17] K. Hara,[51] D. Hare,[48] M. Hare,[52] R. F. Harr,[55] K. Hatakeyama,[5] C. Hays,[39] M. Heck,[24] J. Heinrich,[41] M. Herndon,[56] S. Hewamanage,[5] A. Hocker,[15] W. Hopkins,[15,h] D. Horn,[24] S. Hou,[1] R. E. Hughes,[36] M. Hurwitz,[11] U. Husemann,[57] N. Hussain,[31] M. Hussein,[33] J. Huston,[33] G. Introzzi,[42a] M. Iori,[47b,47a] A. Ivanov,[7,q] E. James,[15] D. Jang,[10] B. Jayatilaka,[14] E. J. Jeon,[25] S. Jindariani,[15] M. Jones,[44] K. K. Joo,[25] S. Y. Jun,[10] T. R. Junk,[15] T. Kamon,[25,49] P. E. Karchin,[55] A. Kasmi,[5] Y. Kato,[38,p] W. Ketchum,[11] J. Keung,[41] V. Khotilovich,[49] B. Kilminster,[15] D. H. Kim,[25] H. S. Kim,[25] J. E. Kim,[25] M. J. Kim,[17] S. B. Kim,[25] S. H. Kim,[51] Y. K. Kim,[11] Y. J. Kim,[25] N. Kimura,[54] M. Kirby,[15] S. Klimenko,[16] K. Knoepfel,[15] K. Kondo,[54,a] D. J. Kong,[25] J. Konigsberg,[16] A. V. Kotwal,[14] M. Kreps,[24] J. Kroll,[41] D. Krop,[11] M. Kruse,[14] V. Krutelyov,[49,d] T. Kuhr,[24] M. Kurata,[51] S. Kwang,[11] A. T. Laasanen,[44] S. Lami,[42a] S. Lammel,[15] M. Lancaster,[28] R. L. Lander,[7] K. Lannon,[36,z] A. Lath,[48] G. Latino,[42c,42a] T. LeCompte,[2] E. Lee,[49] H. S. Lee,[11,r] J. S. Lee,[25] S. W. Lee,[49,cc] S. Leo,[42b,42a] S. Leone,[42a] J. D. Lewis,[15] A. Limosani,[14,u] C.-J. Lin,[26] M. Lindgren,[15] E. Lipeles,[41] A. Lister,[18] D. O. Litvintsev,[15] C. Liu,[43] H. Liu,[53] Q. Liu,[44] T. Liu,[15] S. Lockwitz,[57] A. Loginov,[57] D. Lucchesi,[40b,40a] J. Lueck,[24] P. Lujan,[26] P. Lukens,[15] G. Lungu,[46] J. Lys,[26] R. Lysak,[12,f] R. Madrak,[15] K. Maeshima,[15] P. Maestro,[42c,42a] S. Malik,[46] G. Manca,[27,b] A. Manousakis-Katsikakis,[3] F. Margaroli,[47a] C. Marino,[24] M. Martínez,[4] P. Mastrandrea,[47a] K. Matera,[22] M. E. Mattson,[55] A. Mazzacane,[15] P. Mazzanti,[6a] K. S. McFarland,[45] P. McIntyre,[49] R. McNulty,[27,k] A. Mehta,[27] P. Mehtala,[21] C. Mesropian,[46] T. Miao,[15] D. Mietlicki,[32] A. Mitra,[1] H. Miyake,[51] S. Moed,[15] N. Moggi,[6a] M. N. Mondragon,[15,n] C. S. Moon,[25] R. Moore,[15] M. J. Morello,[42d,42a] J. Morlock,[24] P. Movilla Fernandez,[15] A. Mukherjee,[15] Th. Muller,[24] P. Murat,[15] M. Mussini,[6b,6a] J. Nachtman,[15,o] Y. Nagai,[51] J. Naganoma,[54] I. Nakano,[37] A. Napier,[52] J. Nett,[49] C. Neu,[53] M. S. Neubauer,[22] J. Nielsen,[26,e] L. Nodulman,[2] S. Y. Noh,[25] O. Norniella,[22] L. Oakes,[39] S. H. Oh,[14] Y. D. Oh,[25] I. Oksuzian,[53] T. Okusawa,[38] R. Orava,[21] L. Ortolan,[4] S. Pagan Griso,[40b,40a] C. Pagliarone,[50a] E. Palencia,[9,g] V. Papadimitriou,[15] A. A. Paramonov,[2] J. Patrick,[15] G. Pauletta,[50b,50a] M. Paulini,[10] C. Paus,[30] D. E. Pellett,[7] A. Penzo,[50a] T. J. Phillips,[14] G. Piacentino,[42a] E. Pianori,[41] J. Pilot,[36] K. Pitts,[22] C. Plager,[8] L. Pondrom,[56] S. Poprocki,[15,h] K. Potamianos,[44] F. Prokoshin,[13,dd] A. Pranko,[26] F. Ptohos,[17,i] G. Punzi,[42b,42a] A. Rahaman,[43] V. Ramakrishnan,[56] N. Ranjan,[44] I. Redondo,[29] P. Renton,[39] M. Rescigno,[47a] T. Riddick,[28] F. Rimondi,[6b,6a] L. Ristori,[42a,15] A. Robson,[19] T. Rodrigo,[9] T. Rodriguez,[41] E. Rogers,[22] S. Rolli,[52,j] R. Roser,[15] F. Ruffini,[42c,42a] A. Ruiz,[9] J. Russ,[10] V. Rusu,[15] A. Safonov,[49] W. K. Sakumoto,[45] Y. Sakurai,[54] L. Santi,[50b,50a] K. Sato,[51] V. Saveliev,[15,x] A. Savoy-Navarro,[15,bb] P. Schlabach,[15] A. Schmidt,[24] E. E. Schmidt,[15] T. Schwarz,[15] L. Scodellaro,[9] A. Scribano,[42c,42a] F. Scuri,[42a] S. Seidel,[35] Y. Seiya,[38] A. Semenov,[13] F. Sforza,[42c,42a] S. Z. Shalhout,[7]

T. Shears,[27] P. F. Shepard,[43] M. Shimojima,[51,w] M. Shochet,[11] I. Shreyber-Tecker,[34] A. Simonenko,[13] P. Sinervo,[31] K. Sliwa,[52] J. R. Smith,[7] F. D. Snider,[15] A. Soha,[15] V. Sorin,[4] H. Song,[43] P. Squillacioti,[42c,42a] M. Stancari,[15] R. St. Denis,[19] B. Stelzer,[31] O. Stelzer-Chilton,[31] D. Stentz,[15,y] J. Strologas,[35] G. L. Strycker,[32] Y. Sudo,[51] A. Sukhanov,[15] I. Suslov,[13] K. Takemasa,[51] Y. Takeuchi,[51] J. Tang,[11] M. Tecchio,[32] P. K. Teng,[1] J. Thom,[15,h] J. Thome,[10] G. A. Thompson,[22] E. Thomson,[41] D. Toback,[49] S. Tokar,[12] K. Tollefson,[33] T. Tomura,[51] D. Tonelli,[15] S. Torre,[17] D. Torretta,[15] P. Totaro,[40a] M. Trovato,[42d,42a] F. Ukegawa,[51] S. Uozumi,[25] A. Varganov,[32] F. Vázquez,[16,n] G. Velev,[15] C. Vellidis,[15] M. Vidal,[44] I. Vila,[9] R. Vilar,[9] J. Vizán,[9] M. Vogel,[35] G. Volpi,[17] P. Wagner,[41] R. L. Wagner,[15] T. Wakisaka,[38] R. Wallny,[8] S. M. Wang,[1] A. Warburton,[31] D. Waters,[28] W. C. Wester III,[15] D. Whiteson,[41,c] A. B. Wicklund,[2] E. Wicklund,[15] S. Wilbur,[11] F. Wick,[24] H. H. Williams,[41] J. S. Wilson,[36] P. Wilson,[15] B. L. Winer,[36] P. Wittich,[15,h] S. Wolbers,[15] H. Wolfe,[36] T. Wright,[32] X. Wu,[18] Z. Wu,[5] K. Yamamoto,[38] D. Yamato,[38] T. Yang,[15] U. K. Yang,[11,s] Y. C. Yang,[25] W.-M. Yao,[26] G. P. Yeh,[15] K. Yi,[15,o] J. Yoh,[15] K. Yorita,[54] T. Yoshida,[38,m] G. B. Yu,[14] I. Yu,[25] S. S. Yu,[15] J. C. Yun,[15] A. Zanetti,[50a] Y. Zeng,[14] C. Zhou,[14] and S. Zucchelli[6b,6a]

(CDF Collaboration)

[1]*Institute of Physics, Academia Sinica, Taipei, Taiwan 11529, Republic of China*
[2]*Argonne National Laboratory, Argonne, Illinois 60439, USA*
[3]*University of Athens, 157 71 Athens, Greece*
[4]*Institut de Fisica d'Altes Energies, ICREA, Universitat Autonoma de Barcelona, E-08193, Bellaterra (Barcelona), Spain*
[5]*Baylor University, Waco, Texas 76798, USA*
[6a]*Istituto Nazionale di Fisica Nucleare Bologna, I-40127 Bologna, Italy*
[6b]*University of Bologna, I-40127 Bologna, Italy*
[7]*University of California, Davis, Davis, California 95616, USA*
[8]*University of California, Los Angeles, Los Angeles, California 90024, USA*
[9]*Instituto de Fisica de Cantabria, CSIC-University of Cantabria, 39005 Santander, Spain*
[10]*Carnegie Mellon University, Pittsburgh, Pennsylvania 15213, USA*
[11]*Enrico Fermi Institute, University of Chicago, Chicago, Illinois 60637, USA*
[12]*Comenius University, 842 48 Bratislava, Slovakia; Institute of Experimental Physics, 040 01 Kosice, Slovakia*
[13]*Joint Institute for Nuclear Research, RU-141980 Dubna, Russia*
[14]*Duke University, Durham, North Carolina 27708, USA*
[15]*Fermi National Accelerator Laboratory, Batavia, Illinois 60510, USA*
[16]*University of Florida, Gainesville, Florida 32611, USA*
[17]*Laboratori Nazionali di Frascati, Istituto Nazionale di Fisica Nucleare, I-00044 Frascati, Italy*
[18]*University of Geneva, CH-1211 Geneva 4, Switzerland*
[19]*Glasgow University, Glasgow G12 8QQ, United Kingdom*
[20]*Harvard University, Cambridge, Massachusetts 02138, USA*
[21]*Division of High Energy Physics, Department of Physics, University of Helsinki and Helsinki Institute of Physics, FIN-00014, Helsinki, Finland*
[22]*University of Illinois, Urbana, Illinois 61801, USA*
[23]*The Johns Hopkins University, Baltimore, Maryland 21218, USA*
[24]*Institut für Experimentelle Kernphysik, Karlsruhe Institute of Technology, D-76131 Karlsruhe, Germany*
[25]*Center for High Energy Physics: Kyungpook National University, Daegu 702-701, Korea; Seoul National University, Seoul 151-742, Korea; Sungkyunkwan University, Suwon 440-746, Korea; Korea Institute of Science and Technology Information, Daejeon 305-806, Korea; Chonnam National University, Gwangju 500-757, Korea; Chonbuk National University, Jeonju 561-756, Korea*
[26]*Ernest Orlando Lawrence Berkeley National Laboratory, Berkeley, California 94720, USA*
[27]*University of Liverpool, Liverpool L69 7ZE, United Kingdom*
[28]*University College London, London WC1E 6BT, United Kingdom*
[29]*Centro de Investigaciones Energeticas Medioambientales y Tecnologicas, E-28040 Madrid, Spain*
[30]*Massachusetts Institute of Technology, Cambridge, Massachusetts 02139, USA*
[31]*Institute of Particle Physics: McGill University, Montréal, Québec, Canada H3A 2T8; Simon Fraser University, Burnaby, British Columbia, Canada V5A 1S6; University of Toronto, Toronto, Ontario, Canada M5S 1A7; and TRIUMF, Vancouver, British Columbia, Canada V6T 2A3*
[32]*University of Michigan, Ann Arbor, Michigan 48109, USA*
[33]*Michigan State University, East Lansing, Michigan 48824, USA*
[34]*Institution for Theoretical and Experimental Physics, ITEP, Moscow 117259, Russia*
[35]*University of New Mexico, Albuquerque, New Mexico 87131, USA*
[36]*The Ohio State University, Columbus, Ohio 43210, USA*

[37]*Okayama University, Okayama 700-8530, Japan*
[38]*Osaka City University, Osaka 588, Japan*
[39]*University of Oxford, Oxford OX1 3RH, United Kingdom*
[40a]*Istituto Nazionale di Fisica Nucleare, Sezione di Padova-Trento, I-35131 Padova, Italy*
[40b]*University of Padova, I-35131 Padova, Italy*
[41]*University of Pennsylvania, Philadelphia, Pennsylvania 19104, USA*
[42a]*Istituto Nazionale di Fisica Nucleare Pisa, I-56127 Pisa, Italy*
[42b]*University of Pisa, I-56127 Pisa, Italy*
[42c]*University of Siena, I-56127 Pisa, Italy*
[42d]*Scuola Normale Superiore, I-56127 Pisa, Italy*
[43]*University of Pittsburgh, Pittsburgh, Pennsylvania 15260, USA*
[44]*Purdue University, West Lafayette, Indiana 47907, USA*
[45]*University of Rochester, Rochester, New York 14627, USA*
[46]*The Rockefeller University, New York, New York 10065, USA*
[47a]*Istituto Nazionale di Fisica Nucleare, Sezione di Roma 1, I-00185 Roma, Italy*
[47b]*Sapienza Università di Roma, I-00185 Roma, Italy*
[48]*Rutgers University, Piscataway, New Jersey 08855, USA*
[49]*Texas A&M University, College Station, Texas 77843, USA*
[50a]*Istituto Nazionale di Fisica Nucleare Trieste/Udine, I-34100 Trieste, Italy*
[50b]*University of Udine, I-33100 Udine, Italy*
[51]*University of Tsukuba, Tsukuba, Ibaraki 305, Japan*
[52]*Tufts University, Medford, Massachusetts 02155, USA*
[53]*University of Virginia, Charlottesville, Virginia 22906, USA*
[54]*Waseda University, Tokyo 169, Japan*
[55]*Wayne State University, Detroit, Michigan 48201, USA*
[56]*University of Wisconsin, Madison, Wisconsin 53706, USA*
[57]*Yale University, New Haven, Connecticut 06520, USA*
[58]*LPNHE, Universite Pierre et Marie Curie/IN2P3-CNRS, UMR7585, Paris, F-75252 France*
(Received 20 December 2011; published 2 April 2012)

[a]Deceased.
[b]Visitor from Istituto Nazionale di Fisica Nucleare, Sezione di Cagliari, 09042 Monserrato (Cagliari), Italy.
[c]Visitor from University of California Irvine, Irvine, CA 92697, USA.
[d]Visitor from University of California Santa Barbara, Santa Barbara, CA 93106, USA.
[e]Visitor from University of California Santa Cruz, Santa Cruz, CA 95064, USA.
[f]Visitor from Institute of Physics, Academy of Sciences of the Czech Republic, Czech Republic.
[g]Visitor from CERN, CH-1211 Geneva, Switzerland.
[h]Visitor from Cornell University, Ithaca, NY 14853, USA.
[i]Visitor from University of Cyprus, Nicosia CY-1678, Cyprus.
[j]Visitor from Office of Science, U.S. Department of Energy, Washington, DC 20585, USA.
[k]Visitor from University College Dublin, Dublin 4, Ireland.
[l]Visitor from ETH, 8092 Zurich, Switzerland.
[m]Visitor from University of Fukui, Fukui City, Fukui Prefecture, Japan 910-0017.
[n]Visitor from Universidad Iberoamericana, Mexico D.F., Mexico.
[o]Visitor from University of Iowa, Iowa City, IA 52242, USA.
[p]Visitor from Kinki University, Higashi-Osaka City, Japan 577-8502.
[q]Visitor from Kansas State University, Manhattan, KS 66506, USA.
[r]Visitor from Korea University, Seoul, 136-713, Korea.
[s]Visitor from University of Manchester, Manchester M13 9PL, United Kingdom.
[t]Visitor from Queen Mary, University of London, London, E1 4NS, United Kingdom.
[u]Visitor from University of Melbourne, Victoria 3010, Australia.
[v]Visitor from Muons, Inc., Batavia, IL 60510, USA.
[w]Visitor from Nagasaki Institute of Applied Science, Nagasaki, Japan.
[x]Visitor from National Research Nuclear University, Moscow, Russia.
[y]Visitor from Northwestern University, Evanston, IL 60208, USA.
[z]Visitor from University of Notre Dame, Notre Dame, IN 46556, USA.
[aa]Visitor from Universidad de Oviedo, E-33007 Oviedo, Spain.
[bb]Visitor from CNRS-IN2P3, Paris, F-75205 France.
[cc]Visitor from Texas Tech University, Lubbock, TX 79609, USA.
[dd]Visitor from Universidad Tecnica Federico Santa Maria, 110v Valparaiso, Chile.
[ee]Visitor from Yarmouk University, Irbid 211-63, Jordan.

This paper presents a search for standard model Higgs boson production in association with a W boson using events recorded by the CDF experiment in a data set corresponding to an integrated luminosity of 5.6 fb^{-1}. The search is performed using a matrix element technique in which the signal and background hypotheses are used to create a powerful discriminator. The discriminant output distributions for signal and background are fit to the observed events using a binned likelihood approach to search for the Higgs boson signal. We find no evidence for a Higgs boson, and 95% confidence level (C.L.) upper limits are set on $\sigma(p\bar{p} \to WH) \times \mathcal{B}(H \to b\bar{b})$. The observed limits range from 3.5 to 37.6 relative to the standard model expectation for Higgs boson masses between $m_H = 100$ GeV/c^2 and $m_H = 150$ GeV/c^2. The 95% C.L. expected limit is estimated from the median of an ensemble of simulated experiments and varies between 2.9 and 32.7 relative to the production rate predicted by the standard model over the Higgs boson mass range studied.

DOI: 10.1103/PhysRevD.85.072001 PACS numbers: 14.80.Bn, 13.85.Rm

I. INTRODUCTION

In the standard model (SM), the Higgs mechanism [1–3] is responsible for the spontaneous breaking of the SU(2) × U(1) gauge symmetry which generates the masses of the gauge bosons and more indirectly allows for the fermion masses. This theory predicts the existence of a scalar particle, the Higgs boson, which remains the only SM particle that has not been observed by experiment. Although the Higgs boson mass is not predicted by theory, direct searches done at LEP and Tevatron collider experiments have set limits that constrain the Higgs boson mass to be between 114.4 and 156 GeV/c^2 or above 175 GeV/c^2 at 95% C.L. [4,5]. On the other hand, precision electroweak measurements indirectly constrain its mass to be less than 158 GeV/c^2 at 95% C.L. [6].

At the Tevatron $p\bar{p}$ collider, the Higgs boson is expected to be produced mainly by gluon fusion, while the next most frequent production channel is the associated production of Higgs and W bosons, WH. For Higgs boson masses lower than 135 GeV/c^2, the Higgs boson decay $H \to b\bar{b}$ has the largest branching fraction [7]. The production rate of $b\bar{b}$ pairs from QCD processes is many orders of magnitude larger than Higgs boson production, making the analysis of the process $gg \to H \to b\bar{b}$ nonviable. Associated production $q\bar{q} \to WH$ with the W boson decaying leptonically gives a cleaner signal because requiring a lepton helps to distinguish it from the multijet QCD background [8].

Several searches for a low-mass Higgs boson at the CDF and D0 experiments are combined in order to maximize sensitivity [5]. In that combination, the search in the $\ell\nu b\bar{b}$ final state has proven to be the most sensitive input and therefore carries the most weight in the combination. So, optimizations in this analysis can have an important impact on the ultimate sensitivity of the Tevatron experiments to the Higgs boson.

Recently, the experiments at the Large Hadron Collider (LHC) have obtained enough data to produce search results of similar sensitivity to the Tevatron experiments in the low-mass region [9]. However, at the LHC the most sensitive low-mass search is in the diphoton final state [10] and searches for $H \to b\bar{b}$ will take some time before they reach the sensitivity of the Tevatron combination in this channel [11]. In that sense, the Tevatron and the LHC are quite complementary in that both will provide important information in the search for a low-mass Higgs boson over the next few years.

In this paper, we describe a search for the Higgs boson in the final state where the H is produced in association with a W boson, the Higgs boson decays to $b\bar{b}$, and the W decays to an electron or muon and its associated neutrino. This final state has been investigated before by both Tevatron experiments, CDF and D0 [12,13]. Here we present a new search in a data sample corresponding to an integrated luminosity of 5.6 fb^{-1} and using an optimized discriminant output distribution.

Finding evidence for Higgs boson production in association with a W boson is extremely difficult since the expected production rate is much lower than that of other processes with the same final state, for example $W + b\bar{b}$ and top quark processes. Some of the main challenges of the analysis are the identification and the estimation of these and other background processes and the development of strategies to reduce their contribution while retaining high signal efficiency.

The background processes contributing to the WH final states are $W + b\bar{b}$, $W + c\bar{c}$, $t\bar{t}$, single top, Z + jets, dibosons (WW, WZ, and ZZ), W + jets events, where a jet not originating from a b quark has been misidentified as a heavy-flavor jet, and non-W events where a jet is misidentified as a lepton. These processes have characteristics which differ from those of WH production that will be used to discriminate them from the signal. The background rates are estimated from a combination of simulated and observed events. To distinguish signal from background events a matrix element (ME) technique [14,15] is applied, in which event probability densities for the signal and background hypotheses are calculated and used to create a powerful discriminator. This method was used as part of the observation of single top production [16] and many other analyses within the CDF Collaboration, such as the measurement of the $WW + WZ$ cross section [17], the measurement of the top quark mass [18], the search for

SM Higgs boson production in the WW decay channel [19], and the measurement of the WW production cross section [20].

This paper is organized as follows. Section II briefly describes the CDF II detector [21,22], the apparatus used to collect the observed events used in this analysis. In Sec. III, the identification of the particles and observables that make up the WH final state is presented. Section IV describes the event selection. Identifying b hadrons in jets is essential, and the two algorithms used to identify b jets are presented in Sec. V. The signal and background signatures are discussed in Secs. VI and VII, respectively, together with the method to estimate the total number of events and also the background composition. The matrix element method is described in detail in Sec. VIII. A discussion of systematic uncertainties is included in Sec. IX. Finally, in Secs. X and XI the results and conclusions of the analysis are presented.

II. THE CDF II DETECTOR

The Collider Detector at Fermilab (CDF II) [21,22] is situated at one of the two collision points of the Tevatron $p\bar{p}$ collider. It is a general purpose detector designed to study the properties of these collisions. The detector has both azimuthal and forward-backward symmetry. Since the CDF II detector has a barrel-like shape, we use a cylindrical coordinate system (r, ϕ, z). The origin is located at the center of the detector, r is the radial distance from the beam line and the z axis lies along the nominal direction of the proton beam (toward east). Spherical coordinates (ϕ, θ) are also commonly used, where ϕ is the azimuthal angle around the beam axis and θ is the polar angle defined with respect to the proton beam direction. Pseudorapidity η is defined as $\eta \equiv -\ln[\tan(\theta/2)]$. The transverse energy and momentum of a particle are defined as $E_T = E\sin\theta$ and $p_T = p\sin\theta$, respectively. A diagram of the CDF II detector is shown in Fig. 1. A quadrant of the detector is cut out to expose the different subdetectors.

The CDF II detector consists of three primary subsystems: The innermost part of the detector is the tracking system, which contains silicon microstrip detectors and the central outer tracker (COT), an open cell drift chamber, inside a superconducting solenoid which generates a $1.4T$ magnetic field parallel to the beam axis. These detector systems are designed to reconstruct the trajectories of charged particles and precisely measure their momenta. The silicon detectors provide excellent impact parameter, azimuthal angle, and z resolution [23–25]. For example, the typical intrinsic hit resolution of the silicon detector is 11 μm. The transverse impact parameter (distance of closest approach of a track to the beam line in the transverse plane) resolution is $\sim$40 μm, of which approximately 35 μm is due to the transverse size of the Tevatron interaction region. The entire system reconstructs tracks in three dimensions with the precision needed to identify displaced vertices associated with b and c hadron decays.

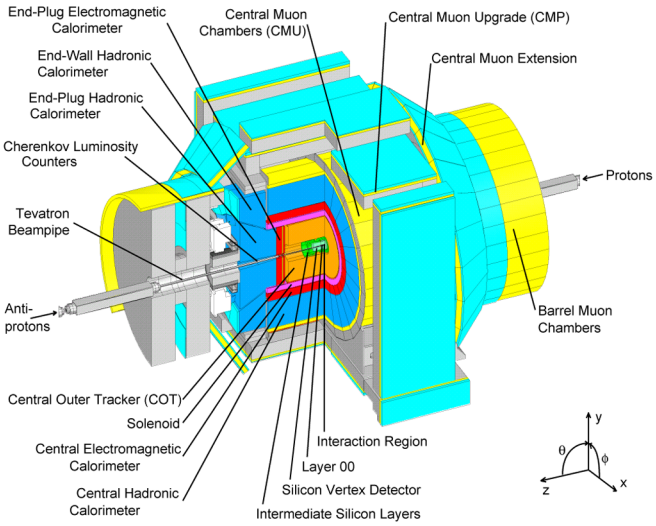

FIG. 1 (color online). A cutaway view of the CDF II detector with quadrant cut to expose the different subdetectors.

The COT [26] provides excellent curvature and angular resolution, with coverage for $|\eta| \leq 1$. The COT has a transverse momentum resolution of $\sigma_{P_T}/P_T^2 = 0.0015\ [\mathrm{GeV}/c]^{-1}$ which improves to $0.0007\ [\mathrm{GeV}/c]^{-1}$ [22] including the silicon detectors. The tracking efficiency of the COT is nearly 100% in the range $|\eta| < 1$, and the coverage is extended to $|\eta| < 1.8$ by including the silicon detectors.

Outside of the solenoid are the calorimeters [27–29], which measure the energy of particles that shower when interacting with matter. The calorimeter is segmented into projective towers, and each tower is divided into an inner electromagnetic and outer hadronic sections. This facilitates separation of electrons and photons from hadrons by the energy deposition profiles as particles penetrate from inner to outer sections. The full array has an angular coverage of $|\eta| < 3.6$. The central region, $|\eta| < 1.1$, is covered by the central electromagnetic calorimeter and the central hadron calorimeter. The central calorimeters have resolutions of $\sigma(E)/E = 13.5\%/\sqrt{E\cdot\sin\theta} \oplus 2\%$ [GeV] and $\sigma(E)/E = 50\%/\sqrt{E} \oplus 3\%$ [GeV] for the electromagnetic and hadronic calorimeters, respectively. The forward region, $1.1 < |\eta| < 3.6$, is covered by the end-plug electromagnetic calorimeter and the end-plug hadron calorimeter, with resolution of $\sigma(E)/E = 16\%/\sqrt{E} \oplus 1\%$ [GeV] and $\sigma(E)/E = 80\%/\sqrt{E} \oplus 5\%$ [GeV] for the plug electromagnetic and hadronic calorimeters, respectively.

Finally, outside of the calorimeters are the muon chambers, which provide muon detection in the range $|\eta| < 1.5$. The muon detectors at CDF [21] make use of single wire drift chambers as well as scintillator counters for fast timing. For the analyses presented in this article, muons are detected in four separate subdetectors. Muons with $p_T > 1.4$ GeV/c penetrating the five absorption lengths of the calorimeter are detected in the four layers of planar

multiwire drift chambers of the central muon detector (CMU) [30]. Behind an additional 60 cm of steel, a second set of four layers of drift chambers, the central muon upgrade (CMP) [31], detects muons with $p_T > 2.2$ GeV/c. The CMU and CMP cover the same part of the central region $|\eta| < 0.6$. The central muon extension (CMX) [31] extends the pseudorapidity coverage of the muon system from 0.6 to 1.0 and thus completes the coverage over the full fiducial region of the COT. Muons in the $|\eta|$ range from 1.0 to 1.5 of the forward region are detected by the barrel muon chambers.

III. DATA SAMPLE AND EVENT RECONSTRUCTION

The data set used in this analysis comes from $p\bar{p}$ collisions at a center-of-mass energy of $\sqrt{s} = 1.96$ TeV recorded by the CDF II detector between 2002 March and 2010 February. The CDF experiment utilizes a three-level trigger system [32–34] to reduce the 1.7 MHz beam crossing rate to ~200 Hz. The first two levels of the trigger system are custom hardware (the second level also has a software component) and the third consists of a farm of computers running a fast version of the offline event reconstruction algorithms.

WH events in the lepton + jets channel are characterized by the presence of an electron or muon with high transverse energy, large missing transverse energy resulting from the undetected neutrino, and two high energy b jets (see Fig. 2).

The data sample used was collected by two trigger strategies, one based on the selection of a high transverse momentum lepton (electron or muon[1] and another one based on missing transverse energy ($\not\!\!E_T$, defined in Sec. III E) + jets.

The total integrated luminosity is 5.6 fb^{-1} for lepton-based triggered events and 5.1 fb^{-1} for muon candidates collected by the $\not\!\!E_T$ + jets trigger. The different luminosities arise from the different detector conditions necessary for each trigger. Electrons reconstructed in the central and end-plug electromagnetic calorimeters are referred to as CEM and PHX electrons, respectively. Muons reconstructed in the central region by the CMU and the CMP detectors are referred to as CMUP muons. Muons detected by the CMX detector are referred to as CMX muons. CEM, PHX, CMUP, and CMX leptons are commonly known as tight leptons and the muons collected by the $\not\!\!E_T$ + jets trigger are known as extended muon coverage (EMC) muons. In this section, we briefly discuss the lepton identification requirements, the reconstruction of jets, and the calculation of $\not\!\!E_T$.

[1]Note that leptonically decaying tau leptons make up a small fraction of our signal acceptance since in this case the tau can be identified as an isolated electron or muon.

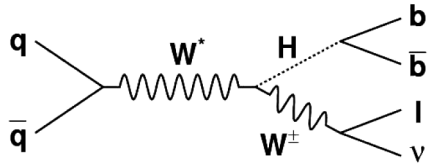

FIG. 2. Feynman diagram showing the final states of the WH process, with leptonic W boson decays. The final state contains a charged lepton, a neutrino, and two b quarks.

A. Electron identification

High-p_T electrons traversing the CDF II detector are expected to leave a track in both the silicon detector and the COT. Subsequently, the electrons will deposit most of their energy into the central or plug electromagnetic calorimeters. The central electron trigger begins by requiring a COT track with $p_T > 9$ GeV/c that extrapolates to an energy cluster of three central electromagnetic calorimeter towers with $E_T > 18$ GeV. Several cuts are then successively applied in order to improve the purity of the electron selection. The reconstructed track with $p_T > 9$ GeV/c must match to an electromagnetic calorimeter cluster with $E_T > 20$ GeV. Furthermore, we require the ratio of hadronic energy to electromagnetic energy $E_{\mathrm{HAD}}/E_{\mathrm{EM}}$ to be less than $0.055 + 0.00045 \times E/\mathrm{GeV}$ and the ratio of the energy of the cluster to the momentum of the track E/pc to be smaller than 2.0 for track momenta ≤ 50 GeV/c.

Electron candidates in the forward direction ($|\eta| > 1.1$, PHX) are defined by a cluster in the plug electromagnetic calorimeter with $E_T > 20$ GeV and $E_{\mathrm{HAD}}/E_{\mathrm{EM}} < 0.05$. The cluster position and the primary vertex position are combined to form a trajectory on which the tracking algorithm utilizes hits in the silicon tracker.

CEM candidates are rejected if an additional high-p_T track is found which forms a common vertex with the track of the electron candidate and has the opposite electric charge since these events are likely to stem from the conversion of a photon.

Figure 3(a) shows the (η, ϕ) distributions of CEM and PHX electron candidates.

B. Muon identification

Muons are characterized by a track in the tracking system, energy deposited in the calorimeter consistent with that of a minimum-ionizing particle, and in cases where they are fiducial to muon chambers they will often leave a track, called a stub, in these detectors. The third-level muon trigger requires a COT track with $p_T > 18$ GeV/c matched to a track segment in the muon chambers.

Muon identification requires an isolated COT track ($p_T > 20$ GeV/c) that extrapolates to a track segment in the muon chambers. Track segments must be detected either in the CMU and the CMP simultaneously (CMUP muons), or in the CMX (CMX muons) for triggered muons. Several additional requirements are imposed in order to

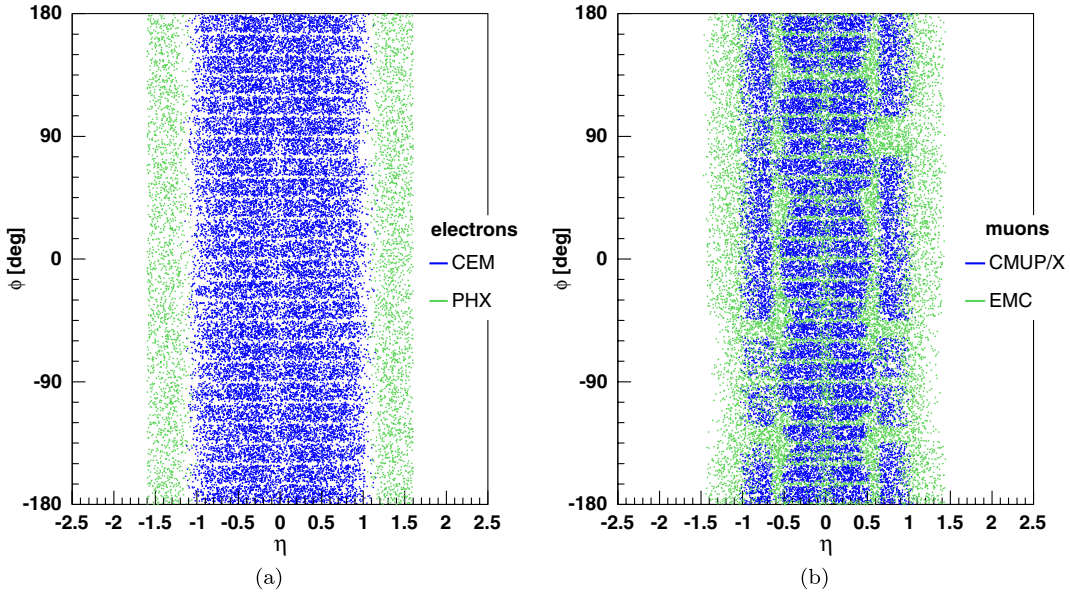

FIG. 3 (color online). Distributions in ($\phi - \eta$) space of the (a) electron and (b) muon selection categories, showing the coverage of the detector that each lepton type provides. The trigger based on $\not\!\!E_T$ plus jets is used to fill in the gaps in the muon trigger coverage.

minimize contamination from hadrons punching through the calorimeter, decays in flight of charged hadrons, and cosmic rays. The energy deposition in the electromagnetic and hadronic calorimeters has to be small, as expected from a minimum-ionizing particle. To reject cosmic-ray muons and muons from in-flight decays of long-lived particles such as K_S^0 and Λ, the impact parameter of the track is required to be less than 0.2 cm if there are no silicon hits on the muon candidate's track, and less than 0.02 cm if there are silicon hits. The remaining cosmic rays are reduced to a negligible level by taking advantage of their characteristic track timing and topology.

In order to add acceptance for events containing muons which are not triggered on directly, several additional muon types are taken from the EMC provided by triggers based on $\not\!\!E_T$ + jets requirements ($\not\!\!E_T > 35$ GeV and the presence of at least two jets). Events passing the $\not\!\!E_T$ + jets trigger are also required to have two sufficiently separated jets: $\Delta R_{jj} > 1$, where $\Delta R \equiv \sqrt{(\Delta\eta)^2 + (\Delta\phi)^2}$. Furthermore, one of the jets must be central, with $|\eta| < 0.9$, and jets are required to have transverse energies above 25 GeV. These additional jet-based requirements remove the dependence of the trigger efficiency to jet observables so that it can be modeled by the $\not\!\!E_T$ alone. The details of the EMC types and selection are included in Ref. [35]. Figure 3(b) shows the (η, ϕ) distribution of all muon candidates.

C. Lepton identification efficiencies

The efficiency of lepton identification is measured using $Z \to e^+e^-$ and $Z \to \mu^+\mu^-$ samples. A pure sample of leptons can be obtained by selecting events where the invariant mass of two high-p_T tracks is near the mass of the Z boson and one track passed the trigger and tight lepton identification selection. The other track can then be examined to see if it also passed the identification cuts to study the efficiency. The same procedure can be applied to simulated Monte Carlo (MC) events and to observed events in the detector and small differences in the efficiencies are observed due to imperfect detector modeling. To correct for this difference, a correction factor is applied to the efficiencies of Monte Carlo events based on the ratio of lepton identification efficiencies calculated from observed events to the efficiency found in Monte Carlo events. The correction factors for the lepton identification are shown in Table I.

D. Jet reconstruction and corrections

Jets consist of a shower of particles originating from the hadronization of highly energetic quarks or gluons. Jets used in this analysis are reconstructed using a cone algorithm [36] by summing the transverse calorimeter energy E_T in a cone of radius $\Delta R \leq 0.4$, for which the E_T of each tower is calculated with respect to the primary vertex z coordinate of the event. The calorimeter towers belonging

TABLE I. Correction factors applied to the Monte Carlo events to correct the lepton identification efficiencies. Since there are different subcategories within the EMC category, we quote the range of variation.

Lepton type	Correction factor
CEM	0.977 ± 0.001
PHX	0.919 ± 0.002
CMUP	0.894 ± 0.002
CMX	0.952 ± 0.002
EMC	0.882 ± 0.003–1.070 ± 0.020

to any electron candidate are not used by the jet clustering algorithm. The energy of each jet is corrected [36] for the η dependence and the nonlinearity of the calorimeter response. The jet energies are also adjusted by subtracting the average extra deposition of energy from additional inelastic $p\bar{p}$ collisions on the same beam crossing as the triggered event.

E. Missing transverse energy reconstruction

The presence of neutrinos in an event is inferred by an imbalance in the transverse components of the energy measurements in the calorimeter. The missing E_T vector ($\vec{\not\!\!E}_T$) is defined by

$$\vec{\not\!\!E}_T = -\sum_i E_T^i \hat{n}_i, \tag{1}$$

where i is the index for the calorimeter tower number with $|\eta| < 3.6$, and $\hat{n}_i$ is a unit vector perpendicular to the beam axis and pointing at the ith calorimeter tower. $\not\!\!E_T$ also refers to the magnitude $|\vec{\not\!\!E}_T|$. The $\not\!\!E_T$ calculation is based on uncorrected tower energies and is then corrected based on the jet-energy corrections of all of the jets in the event. Also the $\not\!\!E_T$ is corrected for the muons, since they traverse the calorimeters without showering. The transverse momenta of all identified muons are added to the measured transverse energy sum and the average ionization energy is removed from the measured calorimeter energy deposits.

IV. EVENT SELECTION

The selection before identifying any jet as a b jet is referred to as pretag and only requires the presence of an electron or muon, $\not\!\!E_T > 20$ GeV (25 GeV in the case of forward electrons) and two or three jets with corrected $E_T > 20$ GeV and $|\eta| < 2.0$. At leading order one expects to have only two high-p_T jets in the final state of WH signal events. However, by allowing for the presence of a third jet, signal acceptance is improved by about 25% due to extra jets mostly produced by gluon radiation in the initial or final state.

In order to reduce the $Z +$ jets, top, and WW/WZ background rates, events with more than one lepton are removed. If one of the leptons is not identified correctly, $Z \rightarrow \ell^+\ell^-$ events still remain. To remove such events, the invariant mass of the lepton and any track with opposite charge must not be in the Z boson mass window $76 < m_{l,\mathrm{track}} < 106$ GeV$/c^2$.

The non-W background consists of multijet events which do not contain W bosons; a description of these background events can be found in Sec. VII B. This non-W background is reduced by applying additional selection requirements which are based on the assumption that these events do not have large $\not\!\!E_T$ from an escaping neutrino, but rather the $\not\!\!E_T$ that is observed comes from lost or mismeasured jets. This requirement has been developed in the framework of the single top observation and is described in detail in [37].

V. b-JET TAGGING ALGORITHMS

The events selected by the above criteria are dominated by the production of W bosons in association with jets. In order to improve the signal-to-background ratio for WH events, at least one of the jets in the event is required to be produced by a b quark. Identifying jets originating from b quarks helps to reduce the background from non-W and $W +$ light flavor ($W + LF$) events. Therefore, the last step of the event selection is the requirement of the presence of at least one b-tagged jet identified using the SECVTX algorithm [38]. In order to increase the acceptance for events with two tagged b jets, an additional b-tagging algorithm that relies on high-impact-parameter tracks within jets, JET PROBABILITY [39], is used. These two tagging algorithms are based on the same principle: the fact that b quarks have a relatively long lifetime and high mass. Therefore, b hadrons formed during the hadronization of the initial b quark can travel a significant distance (on the order of a few millimeters) before decaying to lighter hadrons. Then, the displacement of the b hadron decay point can be detected either directly by vertexing the tracks or indirectly by studying the impact parameters of tracks.

A. Secondary vertex tagger

The SECVTX algorithm looks inside the jet cone to construct secondary vertices using tracks displaced from the primary vertices. The tracks are distinguished by their large impact parameter significance ($|d_0/\sigma_{d_0}|$), where d_0 and σ_{d_0} are the impact parameter and its overall uncertainty. The tracks are fit to a common vertex using a two-pass approach. In the first pass, applying loose track selection criteria ($p_T > 0.5$ GeV$/c$ and $|d_0/\sigma_{d_0}| > 2.5$), the algorithm attempts to reconstruct a secondary vertex which includes at least three tracks (at least one of the tracks must have $p_T > 1$ GeV$/c$). If no secondary vertex is found, the algorithm uses tighter track selection requirements ($p_T > 1$ GeV$/c$ and $|d_0/\sigma_{d_0}| > 3.0$) and attempts to reconstruct a two-track vertex in a second pass. If either pass is successful, the transverse distance (L_{xy}) from the primary vertex of the event is calculated along with the associated uncertainty $\sigma_{L_{xy}}$, which includes the uncertainty on the primary vertex position. Jets are considered as tagged by requiring a displaced secondary vertex within the jet. Secondary vertices are accepted if the transverse decay length significance ($L_{xy}/\sigma_{L_{xy}}$) is greater than or equal to 7.5.

L_{xy} is defined to be positive when the secondary vertex is displaced in the same direction as the jet, and the jet is positively tagged. A negative value of L_{xy} indicates an incorrect b-tag assignment due to misreconstructed tracks. In this case the tag is called negative. These negative tags

are useful for estimating the rate of incorrectly b-tagged jets as explained in Sec. V C.

B. Jet probability tagger

The JET PROBABILITY b-tagging algorithm is also used. Unlike SECVTX, this algorithm does not explicitly require that the tracks form a vertex. Instead, it uses tracks associated with a jet to determine the probability for these to come from the primary vertex of the interaction [39]. The calculation of the probability is based on the impact parameters of the tracks in the jet and their uncertainties. The impact parameter is assigned a positive or negative sign depending on the position of the track's point of closest approach to the primary vertex with respect to the jet direction. It is positive (negative) if the angle ϕ between the jet axis and the line connecting the primary vertex and the track's point of closest approach to the primary vertex itself is smaller (bigger) than $\pi/2$. By construction, the probability for tracks originating from the primary vertex is uniformly distributed from 0 to 1. For a jet coming from heavy-flavor hadronization, the distribution peaks at 0, due to tracks from long-lived particles that have a large impact parameter with respect to the primary vertex. To be considered as tagged, the jets are required to have a value of the JET PROBABILITY variable (P_J) less than 0.05 ($P_J < 5\%$).

C. Tagging efficiencies and mistag rates

The b-tagging efficiencies are needed to estimate the yields of signal and background events, which are obtained from Monte Carlo simulations. The efficiency for identifying a heavy-flavor jet is different in simulated events and in observed events. It is typically overestimated by Monte Carlo models. To correct for this effect, a scale factor is applied to the Monte Carlo tagging efficiency.

The method used to measure the tagging efficiency for heavy-flavor jets is described in detail in [38]. To measure the tagging efficiency in observed events, a calibration sample enriched in heavy flavor is used. This sample is selected by requiring electrons with $p_T > 8$ GeV/c. Along with the electron we require the presence of two jets, the "electron jet" and the "away jet." The electron jet is required to have $E_T > 15$ GeV (including the energy of the electron) and to be within 0.4 of the electron in η-ϕ space (in other words the electron is within the jet cone), and is presumed to contain the decay products of a heavy-flavor hadron. The away jet is required to have $E_T > 15$ GeV and $|\eta| < 1.5$, and it must be approximately back to back with the electron jet ($\Delta\phi > 2$ rad). To measure the tagging efficiency of the heavy-flavor electron jets we employ a double-tag technique, requiring that the away jet be tagged by the corresponding tagging algorithm. This enhances the heavy-flavor fraction of the electron jets and reduces the dependence on the heavy-flavor fraction. The tagging efficiency is also measured for simulated jets by using a Monte Carlo sample similar to the calibration sample. The tagging efficiency ratio of observed events to Monte Carlo simulated events is called the tagging scale factor (SF). The tagging scale factors used in this analysis are summarized in Table II for $P_J < 5\%$ and SECVTX [40]. The uncertainties shown are statistical and systematic.

TABLE II. Tagging scale factors and their uncertainties for $P_J < 5\%$, and SECVTX.

	$P_J < 5\%$	SECVTX
Scale factor	0.806 ± 0.038	0.95 ± 0.04

The probability of misidentifying a light jet as a heavy-flavor jet ("mistag") is closely related to the rate of negatively tagged jets. The negative tag rate is measured in an inclusive-jet sample collected by triggers with various jet E_T thresholds. This tag rate is then parametrized as a six-dimensional tag-rate matrix. The parametrization of the mistag rate is done as a function of three jet variables: transverse energy of the jet (E_T), the number of tracks in the jet ($N_{\rm trk}$), and the pseudorapidity of the jet (η) and three event variables: the sum of the transverse energies of all jets in the event ($\sum E_T^{\rm jet}$), the number of reconstructed vertices in the event ($N_{\rm vtx}$), and the z position of the primary vertex ($z_{\rm vtx}$). These parametrized rates are used to obtain the probability that a given jet will be negatively tagged. It is assumed that the negative tags are due to detector resolution effects only, while positive tags consist of a mixture of heavy-flavor tags, resolution-based mistags of light-flavor jets, and mistags due to K's, Λ's, and nuclear interactions with the detector material. The mistag rate is based on the negative tag rate in the inclusive-jet data, corrected for estimations of the other contributions [40]. Typically, the mistag rate is of the order of a few percent.

D. Splitting tagging categories

As already mentioned, the last step of the event selection is to require the presence of at least one b-tagged jet using the SECVTX algorithm. In order to gain sensitivity, both b-tagging algorithms are used to assign events to one of three nonoverlapping tagging categories, each with a different signal-to-background ratio. The JET PROBABILITY tagger with the cut at 5% is less restrictive than SECVTX. This means that the selection efficiency for real b jets is higher, but it is accompanied by an increase in the background contribution of light jets misidentified as heavy-flavor jets. Some of the events that were not tagged by the SECVTX algorithm are recovered by JET PROBABILITY. The addition of these events translates into a 5% improvement in the final sensitivity of the analysis. Events are selected in the following order: events in which two or more jets are tagged by the SECVTX algorithm (SVSV events), events where only one jet is tagged by SECVTX and the other one is tagged by the JET PROBABILITY algortihm (SVJP

events), and events with only one jet tagged by SECVTX (in this case, none of the other jets is tagged by any of the two algorithms, SVnoJP events).

VI. SIGNAL MODELING AND ACCEPTANCE

Higgs boson events are modeled with the PYTHIA [41] Monte Carlo generator using the CTEQ5L [42] parton distribution functions (PDFs). They are combined with a parametrized response of the CDF II detector [43] and tuned to the Tevatron underlying event data [44].

For this analysis, the Higgs boson mass region where the branching ratio to $b\bar{b}$ is large is studied (Higgs boson masses between 100 and 150 GeV/c^2). Eleven signal MC samples are generated in this range, $100 < m_H < 150$ GeV/c^2 in 5 GeV/c^2 increments.

The number of expected $WH \to \ell\nu_\ell b\bar{b}$ events is given by

$$N = \sigma_{p\bar{p}\to WH} \cdot \mathcal{B}(H \to b\bar{b}) \cdot \varepsilon_{\text{evt}} \cdot \mathcal{L}_{\text{int}}, \quad (2)$$

where $\sigma_{p\bar{p}\to WH}$ is the theoretically predicted cross section of the WH process, $\mathcal{B}$ is the branching ratio of a Higgs boson decaying to $b\bar{b}$, ε_{evt} is the event detection efficiency, and $\mathcal{L}_{\text{int}}$ is the integrated luminosity.

The SM predicted cross sections for WH production and the branching ratios of a Higgs bosons decaying to $b\bar{b}$ for the different Higgs boson masses are calculated to next-to-leading order (NLO) [45] and are quoted in Table III.

The event detection efficiency, ε_{evt}, can be broken down into several factors:

$$\varepsilon_{\text{evt}} = \varepsilon_{z_0} \cdot \varepsilon_{\text{trigger}} \cdot \varepsilon_{\text{lepton Id}} \cdot \varepsilon_{\text{tag}} \cdot \varepsilon_{\text{acc}} \cdot \mathcal{B}(W \to \ell\nu_\ell), \quad (3)$$

where each term corresponds, respectively, to the z vertex cut ($|z| < 60$ cm fiduciality), triggers, lepton identification, b tagging, acceptance requirements, and the branching ratio of the W boson decaying to a lepton and a neutrino. The event detection efficiency is estimated by performing the event selection on the samples of simulated events.

TABLE III. SM branching ratios ($H \to b\bar{b}$) and WH production cross sections for all Higgs boson masses used in this analysis.

Higgs mass (GeV/c^2)	$\mathcal{B}(H \to b\bar{b})$	σ (pb)
100	0.812	0.286
105	0.796	0.253
110	0.770	0.219
115	0.732	0.186
120	0.679	0.153
125	0.610	0.136
130	0.527	0.120
135	0.436	0.103
140	0.344	0.086
145	0.256	0.078
150	0.176	0.070

TABLE IV. Summary of predicted number of signal events based on 5.6 fb^{-1} of integrated luminosity with systematic and statistical uncertainties for each Higgs boson mass in 2-jet events passing all event selection requirements.

Higgs mass (GeV/c^2)	SVSV	SVJP	SVnoJP
100	5.92 ± 0.69	4.12 ± 0.52	15.66 ± 1.23
105	5.50 ± 0.64	3.76 ± 0.47	14.11 ± 1.11
110	4.80 ± 0.56	3.33 ± 0.42	12.34 ± 0.97
115	4.06 ± 0.48	2.80 ± 0.35	10.27 ± 0.81
120	3.24 ± 0.38	2.24 ± 0.28	8.08 ± 0.64
125	2.65 ± 0.31	1.86 ± 0.23	6.59 ± 0.52
130	2.07 ± 0.24	1.44 ± 0.18	5.12 ± 0.40
135	1.49 ± 0.17	1.07 ± 0.13	3.70 ± 0.29
140	1.01 ± 0.12	0.71 ± 0.09	2.46 ± 0.19
145	0.70 ± 0.08	0.50 ± 0.06	1.69 ± 0.13
150	0.44 ± 0.05	0.31 ± 0.04	1.06 ± 0.08

TABLE V. Summary of predicted number of signal events based on 5.6 fb^{-1} of integrated luminosity with systematic and statistical uncertainties for each Higgs boson mass in 3-jet events passing all event selection requirements.

Higgs mass (GeV/c^2)	SVSV	SVJP	SVnoJP
100	1.43 ± 0.17	1.10 ± 0.15	3.36 ± 0.27
105	1.41 ± 0.17	1.06 ± 0.15	3.22 ± 0.26
110	1.29 ± 0.15	0.98 ± 0.13	3.00 ± 0.24
115	1.16 ± 0.14	0.85 ± 0.12	2.57 ± 0.21
120	0.95 ± 0.11	0.71 ± 0.10	2.11 ± 0.17
125	0.81 ± 0.09	0.60 ± 0.08	1.80 ± 0.15
130	0.68 ± 0.08	0.49 ± 0.07	1.44 ± 0.12
135	0.50 ± 0.06	0.37 ± 0.05	1.09 ± 0.09
140	0.35 ± 0.04	0.26 ± 0.04	0.76 ± 0.06
145	0.25 ± 0.03	0.18 ± 0.03	0.54 ± 0.04
150	0.16 ± 0.02	0.12 ± 0.02	0.35 ± 0.03

Control samples in the data are used to calibrate the efficiencies of the trigger, the lepton identification, and the b tagging. These calibrations are then applied to the Monte Carlo samples we use.

The predicted signal yields for the selected two- and three-jet events for each tagging category are estimated by Eq. (2) at each Higgs boson mass point. Tables IV (for two-jet events) and V (for three-jet events) show the number of expected WH events for each Higgs boson mass for an integrated luminosity of 5.6 fb.

VII. BACKGROUND MODELING AND ESTIMATION

Other production processes can mimic the $WH \to \ell\nu_\ell b\bar{b}$ final state. The main contribution comes from heavy-flavor production in association with a leptonic W boson ($Wb\bar{b}$, $Wc\bar{c}$, Wc). $W + LF$ production also gives a

significant contribution due to mistagged jets. Smaller contributions come from electroweak and top quark processes, $t\bar{t}$, single top, diboson production (WW, WZ, ZZ), or Z + jets, and non-W multijet production with misidentified leptons.

In order to estimate the different background rates, a combination of Monte Carlo samples and observed events are used. The observed lepton + jets events consist of electroweak, top (single top and $t\bar{t}$), non-W production, and W + jets processes. Some background processes are estimated based on Monte Carlo simulations scaled to theoretical predictions of the cross section (such as $t\bar{t}$); some are purely data based (non-W); and some require a combination of Monte Carlo and observed events (W + jets). The first step in the background estimate is to calculate the processes that can be reliably simulated using Monte Carlo techniques. Estimating the non-W fraction is the next step. Finally, the observed events that are not non-W, electroweak, or top quark processes are considered to be all W + jets events where b-tag rate estimates from the Monte Carlo are used to estimate the contribution to the b-tagged signal region. Details on each step of this process are given in the sections below.

A. Monte Carlo based background processes

Diboson events (WW, WZ, and ZZ) can contribute to the tagged lepton + jets sample when one boson decays leptonically and the other decays into quarks (Fig. 4). In addition, top pair production in which one lepton [from Fig. 5(a)] or two jets [from Fig. 5(b)] were not reconstructed also constitutes an important background process. The diboson and $t\bar{t}$ simulated events are generated using the PYTHIA [41] Monte Carlo generator. There is a contribution from single top quarks produced in association with a b quark, s-channel [Fig. 6(a)] and t-channel [Fig. 6(b)] single top production. These events are generated using the MADEVENT [46] MC, and the parton showering is done with PYTHIA. Finally, the Z + jets process in which one lepton from Z boson decay is missed [Fig. 7(a)] can also contribute. Z + jets production is simulated using a combination of ALPGEN [47] matrix element generation and PYTHIA parton showering.

The numbers of events from these processes are predicted based on theoretical and measured cross sections, the measured integrated luminosity, and the acceptances and tagging efficiencies derived from Monte Carlo simulations in the same way as the WH process described in Sec. VI. The diboson cross sections are taken from the NLO calculations with Monte Carlo for femtobarn processes (MCFM) [48]. For the Z + jets background, the Z + jets cross section times the branching ratio of Z to charged leptons is normalized to the value measured by CDF [49]. Predictions based on NLO calculations are also used for the $t\bar{t}$ and single top background processes [50,51]. Top cross section predictions assume a top mass of 175 GeV/c^2.

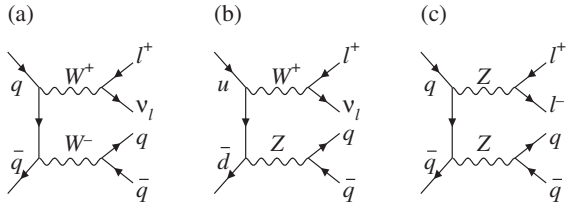

FIG. 4. Feynman diagrams for diboson production (WW, WZ, ZZ), which provides a small background contribution to WH production.

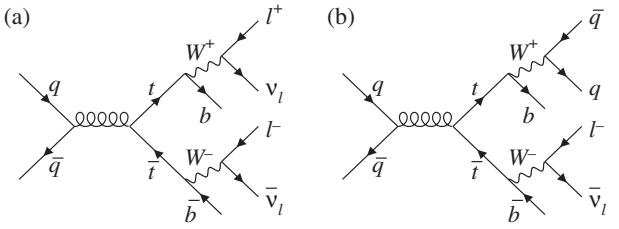

FIG. 5. Feynman diagrams of the $t\bar{t}$ background process to WH production. To pass the event selection, these events must have (a) one charged lepton or (b) two hadronic jets that go undetected.

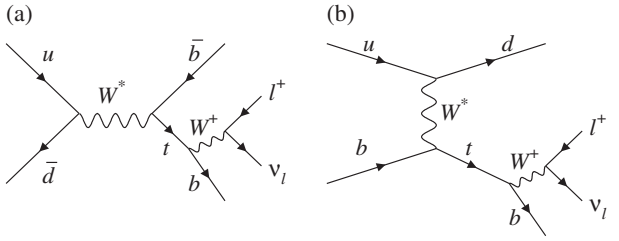

FIG. 6. Feynman diagrams showing the final states of the (a) s-channel and (b) t-channel processes, with leptonic W boson decays. Both final states contain a charged lepton, a neutrino, and two jets, at least one of which originates from a b quark.

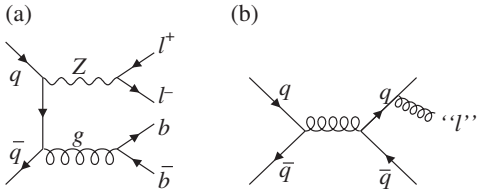

FIG. 7. Representative Feynman diagrams for (a) Z + jets production, where one lepton is missed, and (b) non-W events, in which a jet has to be misidentified as a lepton and $\not{E}_T$ must be mismeasured to pass the event selection. Because the cross section of non-W events is large, they still form a significant background process.

TABLE VI. Summary of predicted numbers of signal ($m_H = 115$ GeV/c^2) and background $W + 2$ jet events passing all the event selection requirements with systematic and statistical uncertainties. The total numbers of observed events passing the event selection are also shown.

Process	SVSV	SVJP	SVnoJP
WW	0.9 ± 0.2	3.3 ± 1.3	106 ± 13
WZ	8.3 ± 1.2	6.2 ± 1.0	35.1 ± 3.9
ZZ	0.30 ± 0.05	0.3 ± 0.1	1.4 ± 0.2
$t\bar{t}$ (lepton + jets)	47.0 ± 7.8	37.6 ± 6.8	205 ± 29
$t\bar{t}$ (dilepton)	28.2 ± 4.6	20.0 ± 3.4	77 ± 11
Single top (t channel)	6.3 ± 1.1	6.3 ± 1.3	116 ± 17
Single top (s channel)	26.2 ± 4.3	18.4 ± 3.1	66.0 ± 9.1
Z + jets	4.2 ± 0.7	5.1 ± 1.3	80 ± 12
$Wb\bar{b}$	142 ± 46	121 ± 39	978 ± 295
$Wc\bar{c}/Wc$	13.8 ± 4.7	46 ± 17	959 ± 296
$W + LF$	4.7 ± 1.5	19 ± 11	946 ± 138
Non-W	19.0 ± 7.6	29 ± 12	298 ± 119
Total prediction	301 ± 53	312 ± 59	3869 ± 619
WH (115 GeV/c^2)	4.06 ± 0.48	2.80 ± 0.35	10.27 ± 0.81
Observed	282	311	3878

TABLE VII. Summary of predicted numbers of signal ($m_H = 115$ GeV/c^2) and background $W + 3$ jets events passing all the event selection requirements with systematic and statistical uncertainties. The total numbers of observed events passing the event selection are also shown.

Process	SVSV	SVJP	SVnoJP
WW	1.0 ± 0.2	2.6 ± 0.9	32.8 ± 4.0
WZ	2.3 ± 0.3	1.9 ± 0.4	9.4 ± 1.1
ZZ	0.19 ± 0.03	0.15 ± 0.03	0.6 ± 0.1
$t\bar{t}$ (lepton + jets)	188 ± 31	161 ± 29	504 ± 70
$t\bar{t}$ (dilepton)	25.4 ± 4.1	18.2 ± 3.1	57.6 ± 8.0
Single top (t channel)	5.6 ± 0.9	5.0 ± 0.9	26.1 ± 3.7
Single top (s channel)	8.9 ± 1.5	6.8 ± 1.2	19.5 ± 2.7
Z + jets	3.0 ± 0.5	4.0 ± 1.1	29.7 ± 4.4
$Wb\bar{b}$	49 ± 16	47 ± 16	258 ± 78
$Wc\bar{c}/Wc$	7.1 ± 2.5	22.9 ± 8.6	237 ± 73
$W + LF$	3.2 ± 1.1	11.3 ± 5.9	255 ± 38
Non-W	9.6 ± 3.9	21.5 ± 8.6	93 ± 37
Total prediction	303 ± 39	303 ± 42	1522 ± 177
WH (115 GeV/c^2)	1.16 ± 0.14	0.85 ± 0.12	2.57 ± 0.21
Observed	318	302	1491

The total diboson (WW, WZ, ZZ), Z + jets, $t\bar{t}$, and single top quark predictions for each tagging category are shown in Tables VI (two-jet events) and VII (three-jet events).

B. Non-W multijet events

The non-W background process consists of events for which the lepton + $\not\!\!E_T$ signature is not due to the decay of a W boson but instead have a fake isolated lepton and mismeasured $\not\!\!E_T$ [Fig. 7(b)]. The main contribution to this source of background comes from QCD multijet production where a jet provides the signature of a lepton and the missing transverse energy is due to a mismeasurement of the jet energies. Semileptonic decays of b hadrons and misidentified photon conversions also contribute. Because of their instrumental nature, these processes cannot be simulated reliably. Therefore, samples of observed events are used to estimate the rates of these processes and model their kinematic distributions.

Three different samples of observed events are used to model the non-W multijet contribution. One sample is based on events that fired the central electron trigger but failed at least two of the five identification cuts of the electron selection requirements that do not depend on the kinematic properties of the event, such as the fraction of energy in the hadronic calorimeter. This sample is used to estimate the non-W contribution from CEM, CMUP, and CMX events. A second sample is formed from events that pass a generic jet trigger with transverse energy $E_T > 20$ GeV to model PHX events. These jets are additionally required to have a fraction of energy deposited in the electromagnetic calorimeter between 80% and 95%, and fewer than four tracks, to mimic electrons. A third sample, used to model the non-W background in EMC events, contains events that are required to pass the $\not\!\!E_T$ + jets trigger (see Sec. III) and contain a muon that passes all identification requirements but failed the isolation requirement. In this case, the isolation is defined as the ratio of the transverse energy surrounding the muon to the transverse energy of the muon. The pseudorapidity distributions of the objects chosen to model the falsely identified lepton must be consistent with that of the sample it is modeling. The first sample works well for central leptons, but cannot cover the PHX or EMC. Highly electromagnetic jets work well for the PHX, while only nonisolated EMC muons give the correct distribution for EMC non-W events.

To estimate the non-W fraction in both the pretag and tagged sample, the $\not\!\!E_T$ spectrum is fit to a sum of the predicted background shapes, as described in detail elsewhere [37]. The fit has one fixed component and two templates whose normalizations can float. The fixed component is coming from the Monte Carlo based processes. The two floating templates are a Monte Carlo W + jets template and a non-W template. The non-W template is different depending on the lepton category, as explained above. The pretag non-W fraction is used to estimate the heavy-flavor and light-flavor fractions.

The total non-W contribution for each tagging category is shown in Tables VI and VII.

C. W + heavy flavor contributions

W + heavy flavor production is the main source of background in the tagged lepton + jets sample. W + jets

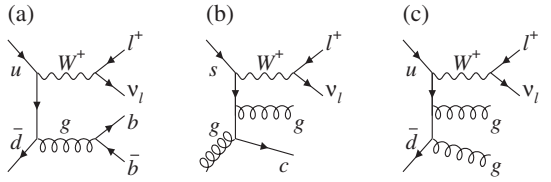

FIG. 8. Some representative diagrams of W + jets production. $Wc\bar{c}$ is the same process as $Wb\bar{b}$, but with charm quarks replacing the b quarks.

production is simulated using a combination of ALPGEN matrix element generation and PYTHIA parton showering (same as for Z + jets events). Diagrams for some of the sample processes included in ALPGEN are shown in Fig. 8.

The contribution of this background is estimated using the heavy-flavor fractions in W + jets production and the tagging efficiencies for these processes. These quantities are derived from Monte Carlo simulations as explained in [37]. The contribution of W + heavy flavor events to our signal region is calculated by

$$N^{\text{tag}}_{W+\text{HF}} = (N^{\text{pretag}}_{\text{data}} \cdot (1 - f^{\text{pretag}}_{\text{non-}W}) - N^{\text{pretag}}_{\text{MC}}) \cdot f_{hf} \cdot k \cdot \varepsilon_{\text{tag}}, \tag{4}$$

where $N^{\text{pretag}}_{\text{data}}$ is the number of observed events in the pretag sample, $f^{\text{pretag}}_{\text{non-}W}$ is the fraction of non-W events in the pretag sample, as determined from the fits described in Sec. VII B, and $N^{\text{pretag}}_{\text{MC}}$ is the expected number of pretag events in Monte Carlo based samples. The fraction of W-boson events with jets matched to heavy-flavor quarks, f_{hf}, is calculated from Monte Carlo simulation. This fraction is multiplied by a scale factor, $k = 1.4 \pm 0.4$, to account for differences between the heavy-flavor fractions observed in data and the Monte Carlo prediction. The k factor is primarily calculated in the one-jet control sample and applied to all jet multiplicities. ε_{tag} is the tagging selection efficiency. See Ref. [37] for more detail.

D. Rates of events with mistagged jets

The other W + jets contribution which can mimic the $\ell\nu_\ell b\bar{b}$ final state is $W + LF$. In this case, jets from light partons tagged as heavy-flavor jets can contribute to the tagged sample. We count the events in the pretag sample and apply a mistag matrix to calculate the fraction of W + light flavor events that will be mistagged ($N_{\text{mistag}}/N_{\text{pretag}}$). The mistag rate parametrization is described in Sec. V C. Then, in order to only use mistagged events from $W + LF$ processes, we subtract the fraction of pretag events which are due to non-W, electroweak, top quark, and W + heavy flavor processes from the pretag sample. The predicted number of background events from $W + LF$ processes is then calculated as

$$N^{\text{tag}}_{W+LF} = (N^{\text{pretag}}_{\text{data}} \cdot (1 - f^{\text{pretag}}_{\text{non-}W}) - N^{\text{pretag}}_{\text{MC}} - N^{\text{pretag}}_{W+\text{HF}}) \cdot \frac{N_{\text{mistag}}}{N_{\text{pretag}}}. \tag{5}$$

The total $Wb\bar{b}$, $Wc\bar{c}/Wc$, and $W + LF$ contributions for each tagging category are shown in Tables VI and VII.

E. Summary of background estimation

The contributions of individual background sources have been described in this section. The summary of the background and signal ($m_H = 115$ GeV/c^2) estimates and the number of observed events are shown for the three different tagging categories in Tables VI and VII. The numbers of expected and observed events are also shown in Fig. 9 as a function of jet multiplicity. In these tables and plots, all lepton types are combined. In general, the numbers of expected and observed events are in good agreement within the uncertainties on the background predictions.

F. Validation of the background model

Since the analysis described here relies on Monte Carlo simulation, the result depends on the proper modeling of

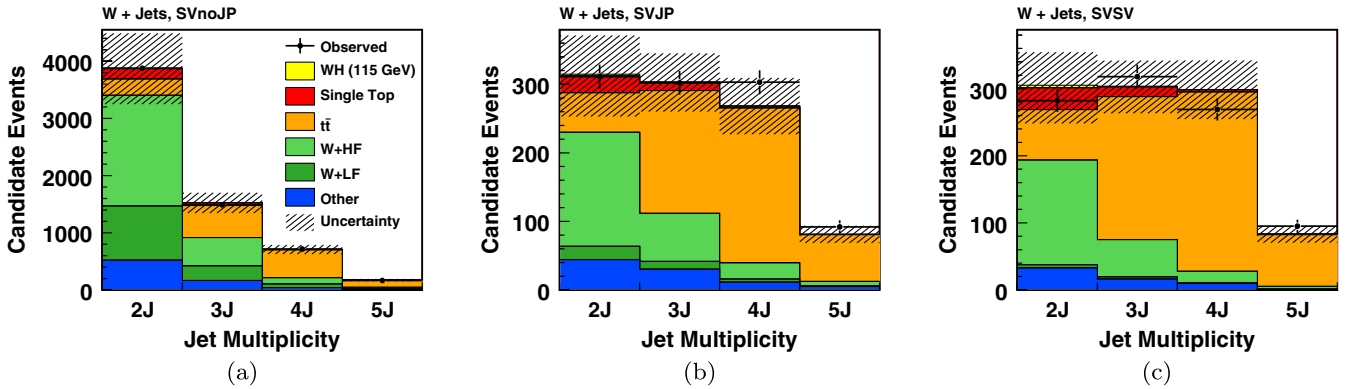

FIG. 9 (color online). The predicted and observed number of events for lepton + jets events. The observed events are indicated with points, and the shaded histograms show the signal and background predictions which are stacked to form the total prediction. Other is the sum of the WW, WZ, ZZ, and Z + jets contributions and W + HF is the sum of the $Wb\bar{b}$, $Wc\bar{c}$, and Wc contributions. (a) SVnoJP, (b) SVJP, and (c) SVSV events.

the signal and the background processes. For that reason, the prediction of the background model is compared with the observed events for hundreds of distributions in the signal region and in different control regions. Figures 10–12 show examples of validation plots for two and three jet bins, in a control region with no b-tagged jets (to check the $W + LF$ shapes) and in the signal region with at least one tagged jet. In general, the agreement is good.

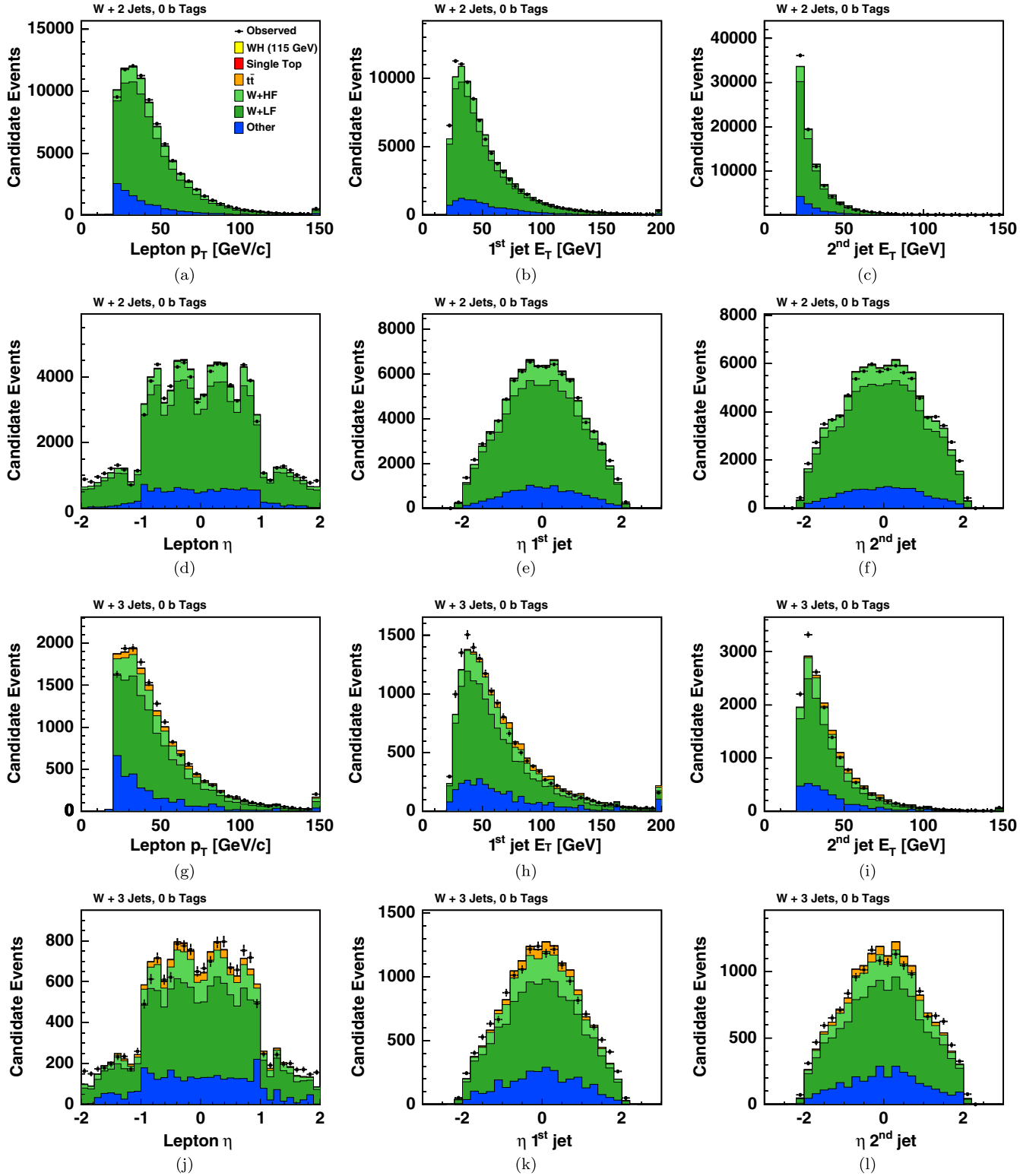

FIG. 10 (color online). Validation plots comparing observed events and Monte Carlo distributions for basic kinematic quantities for events with (a)–(f) two and (g)–(l) three jets and no b tags. The observed events are indicated with points.

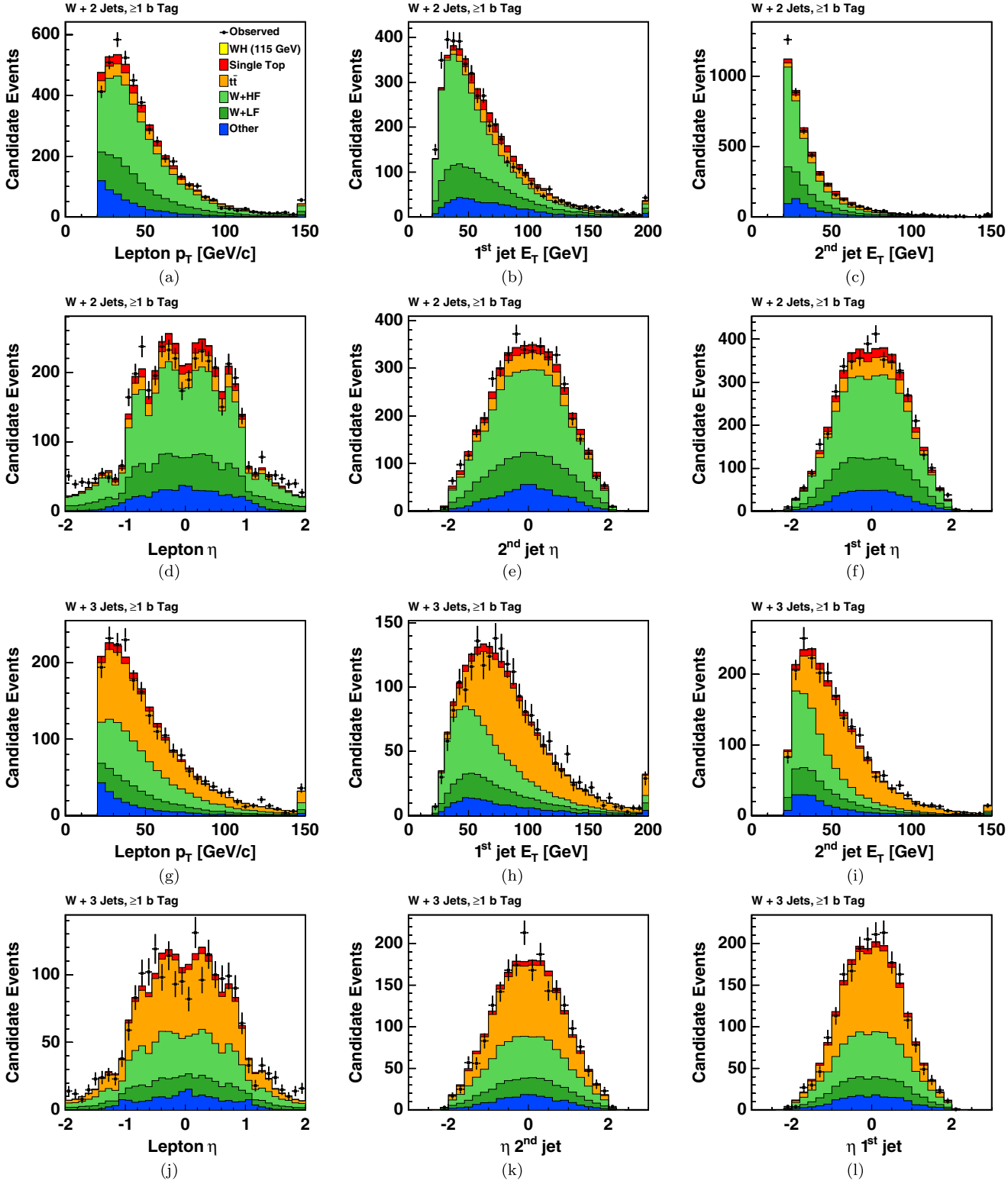

FIG. 11 (color online). Validation plots comparing observed events and Monte Carlo distributions for basic kinematic quantities for events with (a)–(f) two and (g)–(l) three jets and at least one b tag. The observed events are indicated with points.

The lepton and jet transverse energy distributions are the least well modeled. To check the effect of this mismodeling we derive weights from the lepton and jet transverse energies in the control region, and we have applied them to the discriminant variable in the signal region. We check the effect of each variable one at a time by calculating the expected limits in each case and found that the effect on the result was not significant. The validation of

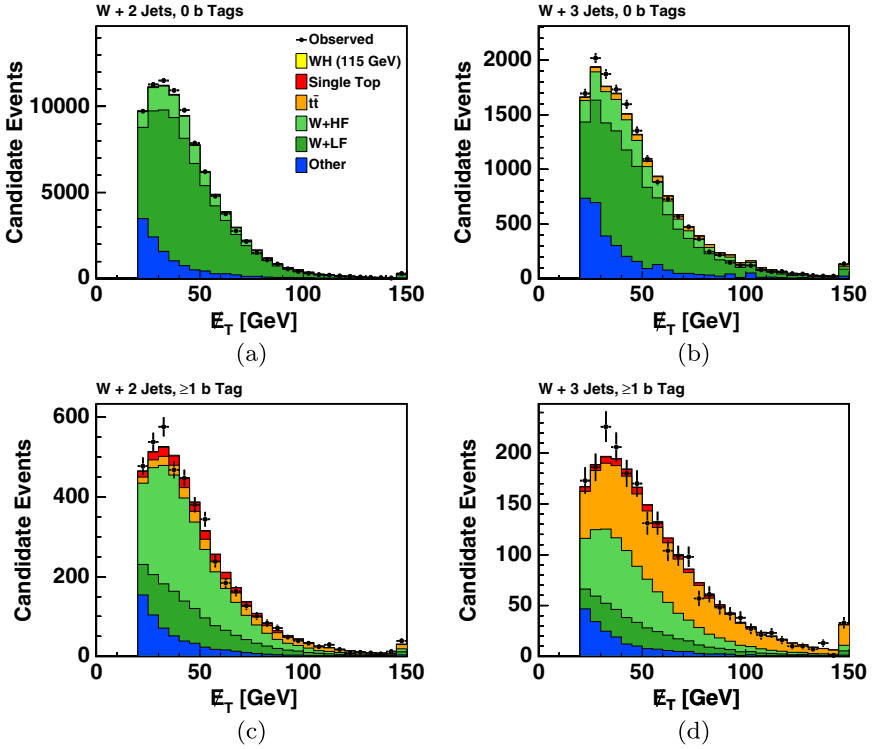

FIG. 12 (color online). Validation plots comparing observed events and Monte Carlo distributions for missing transverse energy for events with (a), (c) two and (b), (d) three jets, with no b tags (top panels) and with at least one b tag (bottom panels). The observed events are indicated with points.

the modeling of other observable quantities is shown later in this paper.

VIII. MATRIX ELEMENT METHOD

The number of expected signal events after the initial selection is much smaller than the uncertainty in the background prediction. For example, for a Higgs boson mass of 115 GeV$/c^2$ the signal-to-background ratio is at best only about $1/70$ even in the most signal rich b-tagging categories. Thus, a method based only on counting the total number of events is unsuitable. The invariant mass distribution of the two leading jets in the event is the most powerful variable for discriminating signal from background, but it is limited by the jet-energy resolution. Figure 13 shows the invariant mass distribution of the two leading jets for two-jet SVSV events. Further discrimination between signal and background is needed.

A ME method [14,15] is used in this search to discriminate signal from background events. This multivariate method relies on the evaluation of event probability densities (commonly called event probabilities) for signal and background processes based on calculations of the relevant standard model differential cross sections. The ratio of signal and background event probabilities is then used as a discriminant variable called the event probability discriminant (EPD). The goal is to maximize sensitivity through the use of all kinematic information contained in each event analyzed. The discriminant distributions are optimized separately for each Higgs boson mass hypothesis in order to extract the maximum sensitivity. Using the EPD as the discriminant variable leads to an increase in sensitivity of $\sim$20% with respect to only using the invariant mass distribution of the two leading jets in the event.

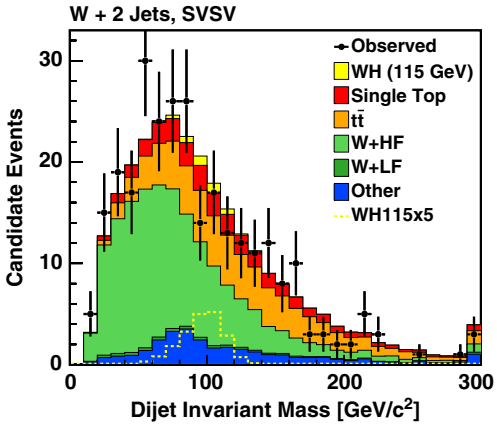

FIG. 13 (color online). Invariant mass distribution of the two leading jets for 2-jet SVSV events. The Higgs boson signal contribution ($M_H = 115$ GeV$/c^2$) is multiplied by a factor of 5 to make it visible.

A. Event probability

If we could measure the four-vectors of the initial and final state particles precisely, the event probability would be

$$P_{\text{evt}} \sim \frac{d\sigma}{\sigma}, \tag{6}$$

where the differential cross section is given by [52]

$$d\sigma = \frac{(2\pi)^4 |\mathcal{M}|^2}{4\sqrt{(q_1 \cdot q_2)^2 - m_{q_1}^2 m_{q_2}^2}} d\Phi_n(q_1 + q_2; p_1, \ldots, p_n), \tag{7}$$

where $\mathcal{M}$ is the Lorentz-invariant matrix element; q_1, q_2 and m_{q_1}, m_{q_2} are the four momenta and masses of the incident particles; $p_1 - p_n$ are the four momenta of the final particles, and $d\Phi_n$ is the n-body phase space given by [52]

$$d\Phi_n = \delta^4\left(q_1 + q_2 - \sum_{i=1}^{n} p_i\right) \prod_{i=1}^{n} \frac{d^3 p_i}{(2\pi)^3 2E_i}. \tag{8}$$

However, several effects have to be considered: (1) the partons in the initial state cannot be measured, (2) neutrinos in the final state are not measured directly, and (3) the energy resolution of the detector cannot be ignored. To address the first point, the differential cross section is weighted by parton distribution functions. To address the second and third points, we integrate over all particle momenta which we do not measure (the p_z of the neutrino), or do not measure well, due to resolution effects (the jet energies). The integration gives a weighted sum over all possible parton-level variables y leading to the observed set of variables x measured with the CDF detector. The mapping between the particle variables y and the measured variables x is established with the transfer function $W(y, x)$, which encodes the detector resolution and is described in detail in Sec. VIII B. Thus, the event probability now takes the form:

$$P(x) = \frac{1}{\sigma} \int d\sigma(y) dq_1 dq_2 f(y_1) f(y_2) W(y, x), \tag{9}$$

where $d\sigma(y)$ is the differential cross section in terms of the particle variables; $f(y_i)$ are the parton distribution functions, with y_i being the fraction of the proton momentum carried by the parton ($y_i = E_{q_i}/E_{\text{beam}}$); and $W(y, x)$ is the transfer function. Substituting Eqs. (7) and (8) into Eq. (9), and considering a final state with four particles ($n = 4$), transforms the event probability to

$$P(x) = \frac{1}{\sigma} \int 2\pi^4 |\mathcal{M}|^2 \frac{f(y_1)}{|E_{q_1}|} \frac{f(y_2)}{|E_{q_2}|} W(y, x) d\Phi_4 dE_{q_1} dE_{q_2}, \tag{10}$$

where the masses and transverse momenta of the initial partons are neglected [i.e., $\sqrt{(q_1 \cdot q_2)^2 - m_{q_1}^2 m_{q_2}^2} \simeq 2E_{q_1} E_{q_2}$].

The squared matrix element $|\mathcal{M}|^2$ for the event probability is calculated at leading order by using the HELAS (helicity amplitude subroutines for Feynman diagram evaluations) package [53]. The subroutine calls for a given process are automatically generated by MADGRAPH [46]. For events with two jets, event probability densities for the WH signal (for 11 Higgs boson masses), as well as for the s-channel and t-channel single top, $t\bar{t}$, $Wb\bar{b}$, $Wc\bar{c}$, Wc, mistags (Wgj, and Wgg) and diboson (WW, WZ) background processes are calculated. The WH channel is mainly produced in two-jet events, but it can happen that an initial or final state radiation jet is identified as the third jet of the event. Including three-jet events increases signal acceptance and gains sensitivity to the Higgs boson signal. In the case of events with three jets in the final state, event probability densities for the WH signal, as well as for the s-channel and t-channel single top, $t\bar{t}$, $Wb\bar{b}$, and $Wc\bar{c}$ processes are calculated. The WH Feynman diagrams include only those with initial and final state radiation, and exclude those in which a ggH coupling is present as these contribute less than 1% to the total cross section, but increase the computation time by more than 20%.

The integration performed in the matrix element calculation of this analysis is identical to the one for the search for single top production [37]. The matrix elements correspond to fixed-order tree-level calculations and thus are not perfect representations of the probabilities for each process. This limitation of the matrix element calculations for the discriminant affects the sensitivity of the analysis but not its correctness, as the same matrix elements are calculated for both observed and Monte Carlo events, which uses parton showers to approximate higher-order effects on kinematic distributions. The different combinations of matching jets to quarks are also considered [54].

A data-MC comparison of the measured four vectors can be found in Figs. 14 and 15. This comparison is done in the control (0 tag) and signal (≥ 1 tag) regions. In general, good agreement between observed data and MC expectation is found.

B. Transfer functions

The transfer function $W(y, x)$ gives the probability of measuring the set of observable variables x given specific values of the parton variables y. In the case of well-measured quantities, $W(y, x)$ is taken as a δ function (i.e., the measured momenta are used in the differential cross section calculation). When the detector resolution cannot be ignored, $W(y, x)$ is a parametrized resolution function based on fully simulated Monte Carlo events. For unmeasured quantities, such as the three components of the momentum of the neutrino, the transfer function is constant. The choice of transfer function affects the sensitivity of the analysis but not its correctness, since the same transfer function is applied to both observed and Monte Carlo events.

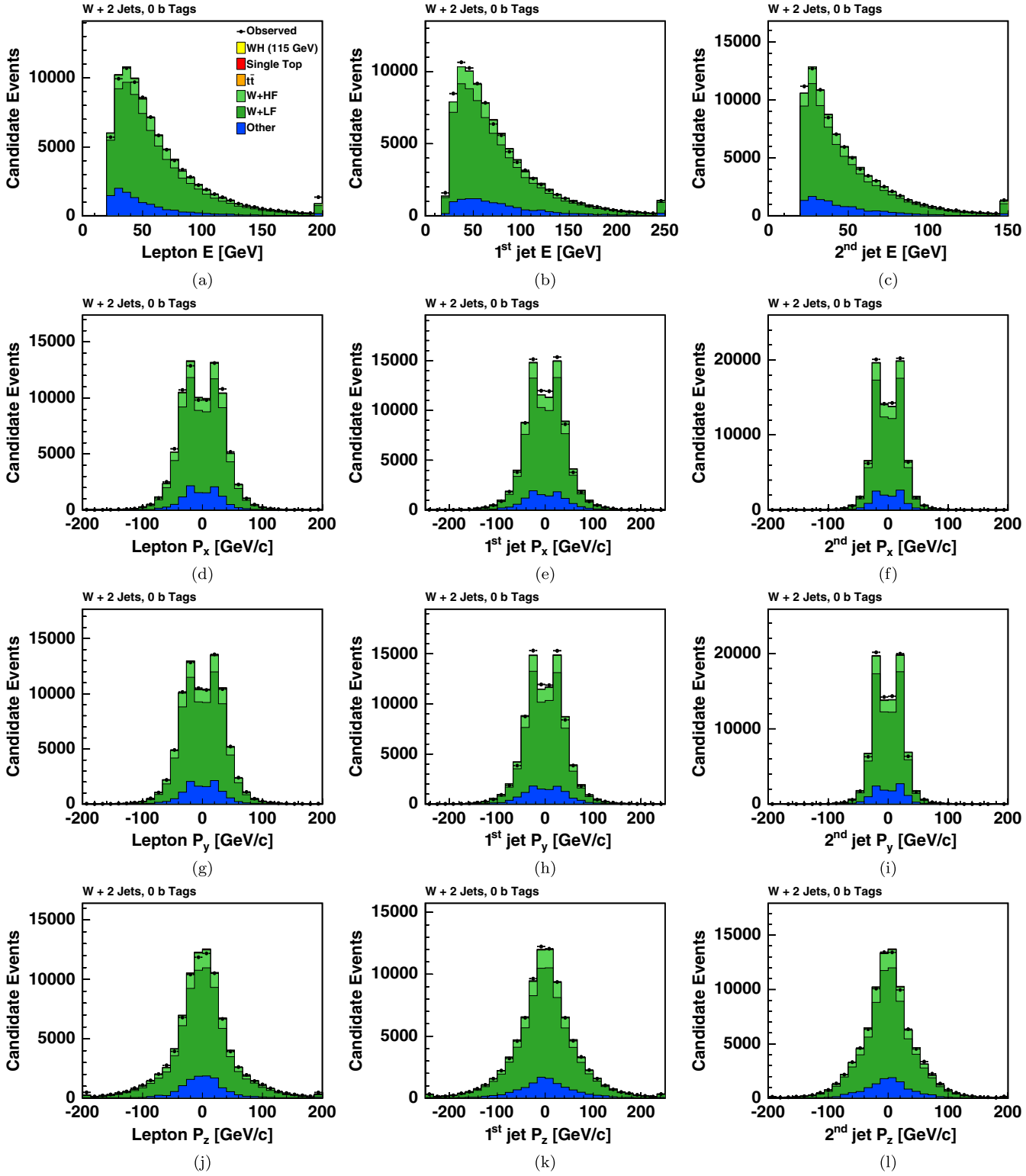

FIG. 14 (color online). Validation plots comparing observed and MC simulated events for the four-vector (E, P_x, P_y, P_z) of the lepton and the jets in 2-jet untagged events.

Lepton energies are measured well by the CDF detector and δ functions are assumed for their transfer functions. The angular resolution of the calorimeter and muon chambers is also sufficient and δ functions are also assumed for the transfer function of the lepton and jet directions. The resolution of jet energies, however, is broad and it is described by a jet transfer function $W_{\text{jet}}(E_{\text{parton}}, E_{\text{jet}})$. Using these assumptions, $W(y, x)$ takes the following

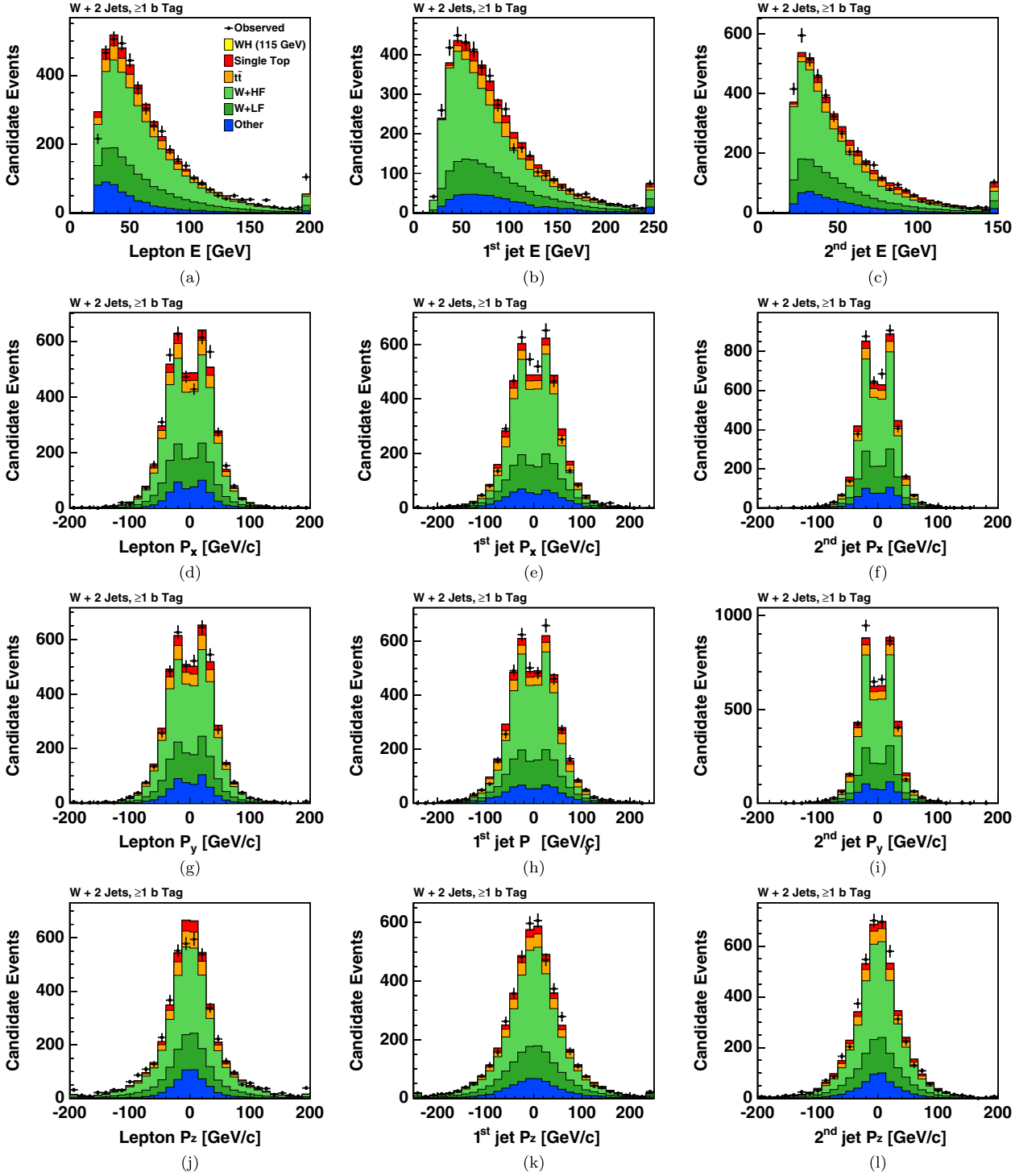

FIG. 15 (color online). Validation plots comparing observed and MC simulated events for the four-vector (E, P_x, P_y, P_z) of the lepton and the jets in events with 2-jets and at least one b-tagged jet.

form for the four final state particles considered in the WH search (lepton, neutrino, and two jets):

$$W(y,x) = \delta^3(\vec{p}_l^{\,y} - \vec{p}_l^{\,x}) \prod_{i=1}^{2} \delta^2(\Omega_i^y - \Omega_i^x) \prod_{k=1}^{2} W_j(E_{p_k}, E_{j_k}), \tag{11}$$

where $\vec{p}_l^{\,y}$ and $\vec{p}_l^{\,x}$ are the produced and measured lepton momenta, Ω_i^y and Ω_i^x are the produced quark and measured jet angles ($\cos\Theta$, ϕ), and E_{p_k} and E_{j_k} are the produced quark and measured jet energies.

The jet-energy transfer functions map parton energies to measured jet energies after correction for instrumental

detector effects [36]. This mapping includes effects of radiation, hadronization, measurement resolution, and energy outside the jet cone not included in the reconstruction algorithm. The jet transfer functions are obtained by parametrizing the jet response in fully simulated Monte Carlo events. The distributions of the difference between the parton and jet energies, $\delta_E = (E_{\text{parton}} - E_{\text{jet}})$, are parametrized as a sum of two Gaussian functions:

$$W_{\text{jet}}(E_{\text{parton}}, E_{\text{jet}}) = \frac{1}{\sqrt{2\pi}(p_2 + p_3 p_5)}\left(\exp\frac{-(\delta_E - p_1)^2}{2p_2^2} + p_3 \exp\frac{-(\delta_E - p_4)^2}{2p_5^2}\right), \quad (12)$$

one to account for the sharp peak and the other one to account for the asymmetric tail, because the δ_E distributions (shown in Fig. 16 for different flavor jets) are asymmetric and feature a significant tail at positive δ_E.

Different transfer functions are created depending on the physics process and the flavor of the jet due to the different kinematics as shown in Fig. 16. To take into account the different kinematics of the physics processes used in this analysis ($WH[100–150]$ GeV$/c^2$, $Wb\bar{b}$, $t\bar{t}$, s-channel and t-channel single top, $Wc\bar{c}$, Wcg, Wjg, Wgg, WW, and WZ) and the different flavor of jet (b, c, light and gluons), 23 different transfer functions are created as explained below.

One of the novelties of this analysis is that, in order to better reproduce the parton energy (E_{parton}), a neural network output (O_{NN}) is used instead of the measured jet energy (E_{jet}). This output distribution is not a neural network output event classifier distribution, but rather a functional approximation to the parton energy. So $W_{\text{jet}}(E_{\text{parton}}, E_{\text{jet}})$ is substituted for $W_{\text{jet}}(E_{\text{parton}}, O_{\text{NN}})$, and it is commonly referred to as a neural network transfer function (or NNTF). The O_{NN} used in the analysis is the result of training neural networks (NNs) using the Stuttgart neural network simulator (SNNS) [55]. For each physics process considered, a different NN is constructed for each type of jet in that process as shown in Table VIII. By using the jets from the specific process to train the NN it is assured that the NN is optimized for the kinematics of the jets associated with that process.

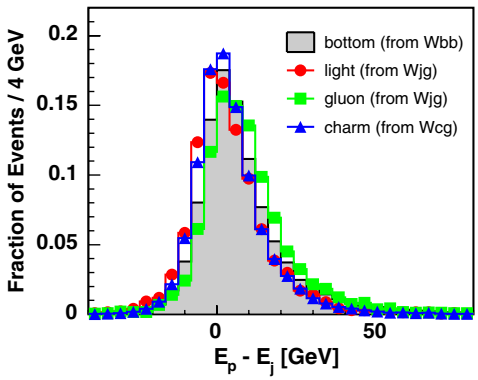

FIG. 16 (color online). Normalized $\delta_E = (E_{\text{parton}} - E_{\text{jet}})$ distributions for jets matched to partons in WH with a Higgs boson mass of 115 GeV$/c^2$ (b-jets), W_{jg} (light-jets and gluons), and W_{cg} (c-jets) Monte Carlo events (passed through full detector simulation).

The training of the NNs is based on MC simulated events. The MC events used for the trainings are the remaining events after applying the analysis event selection (see Sec. IV) and the jets are required to be aligned within a cone of $\Delta R < 0.4$ with the closest flavored parton (b or c depending on the physics process) coming from the hard scattering process.

All the NN trainings have the same architecture and input variables. Seven input variables related to the jet kinematics have been used: the total corrected energy of the jet (E), the raw (measured) transverse momentum of the jet (p_T), the azimuthal angle of the jet (ϕ), the pseudorapidity of the jet (η), the raw (measured) energy of the jet, the total corrected energy of the jet in a cone of radius $R \leq 0.7$ (E cone 0.7), and the sum over the tracks in the jet of the ratio of the transverse momentum of the track and the sine of the θ of the track ($\sum_p$).

Figure 17 shows the data-MC comparison of the seven input variables for the leading jet in two-jet events where at least one of the jets has been tagged by SECVTX which also validates the MC expectations in this signal region.

Figure 18 shows the difference between the parton energy and the corrected jet energy and between the parton energy and the O_{NN} for four different physics processes, WH, diboson (WW, WZ), $Wb\bar{b}$, and Wgg. In all cases the average O_{NN} is closer to the parton energy than the average corrected jet energy and the distributions are more narrow. Therefore, since the O_{NN} provides a better jet resolution, using it as an input to the transfer function should help to improve the performance of the transfer function.

The functional form used to parametrize E_{parton}-O_{NN} is the same as the one described above for δ_E [Eq. (12)]. More details on the performance of the NNTF can be found in Ref. [56].

TABLE VIII. Types of jets used to train the different NNs for each process.

Process	b jets	c jets	Light jets	Gluons
WH (11 m_H values)	X			
$Wb\bar{b}$	X			
$Wc\bar{c}$		X		
$t\bar{t}$	X			
s channel	X			
t channel	X		X	
Wcg		X		X
Wjg			X	X
Wgg				X
$WW - WZ$			X	

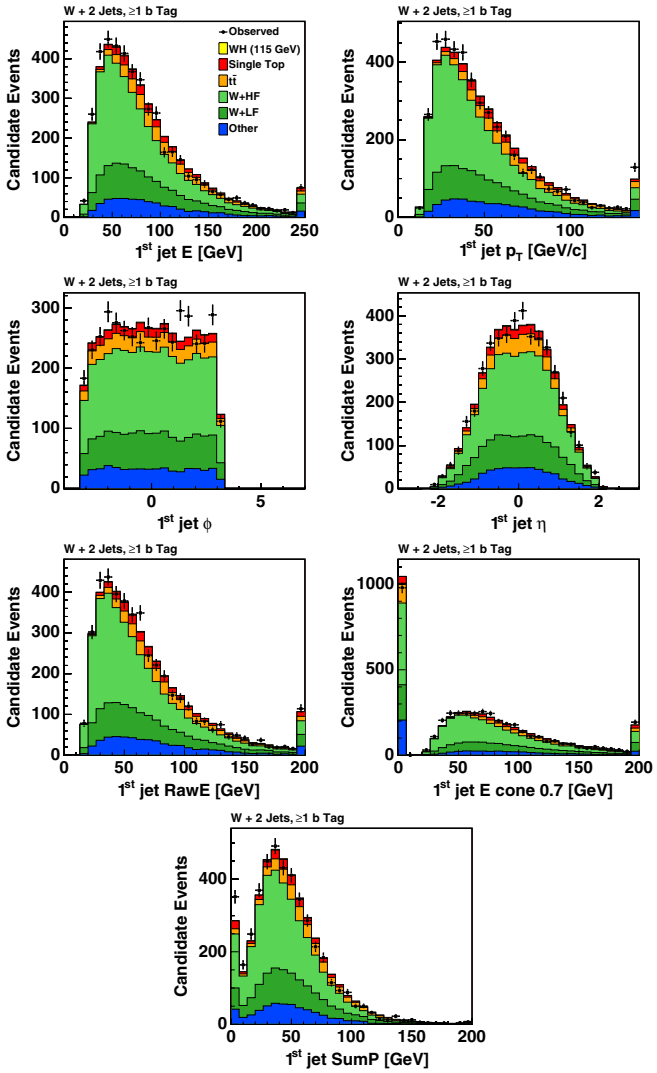

FIG. 17 (color online). Validation plots comparing observed and Monte Carlo simulated events for the seven input variables of the neural network transfer function for the first leading jet for events with two jets and at least one b tag. The observed events are indicated with points.

The output of the neural network is used to correct the measured energy of all the jets from the events that pass the analysis selection. As a cross-check, a comparison of the invariant mass resolution of the dijet system in WH signal events before and after applying this correction is performed. A way to do this is to fit the invariant mass distribution to a Gaussian function and compare the resolution, defined as the sigma divided by the mean of the fit, for all Higgs boson masses. The results are shown in Fig. 19 (left panel). As expected, the invariant mass resolution is better (smaller sigma) after correcting by the O_{NN}. The linearity of the correction is also checked; see Fig. 19 (right panel). Both functions are linear. The only difference is that the reconstructed invariant mass is closer to the generated one once the correction is applied.

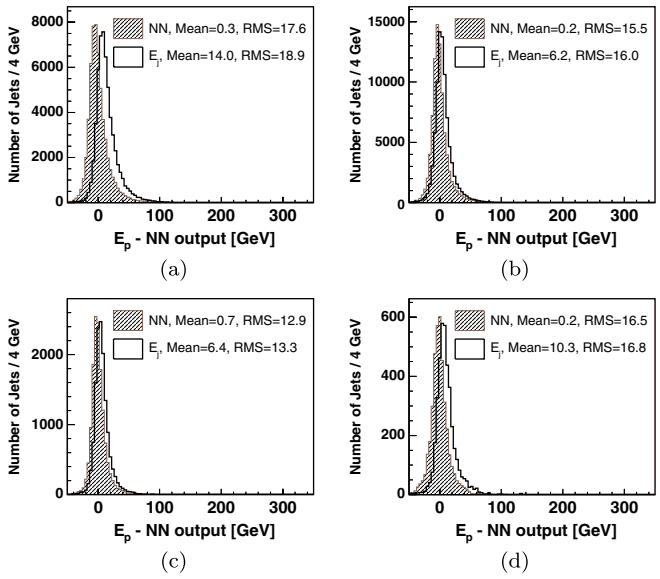

FIG. 18 (color online). Difference between the parton energy and the measured jet energy (empty histogram) and the O_{NN} (dashed histogram) for b jets in (a) WH ($m_H = 115$ GeV/c^2) events, (b) b jets in $Wb\bar{b}$ events, (c) light jets in diboson (WW, WZ) events, and (d) Wgg events for gluon.

C. Event probability discriminant

The event probability densities are used as inputs to build an event probability discriminant, a variable for which the distributions of signal events and background events are maximally different.

An intuitive discriminant which relates the signal and background probability densities is the ratio of signal probability over signal plus background probability, $\mathrm{EPD} = P_{\mathrm{signal}}/(P_{\mathrm{signal}} + P_{\mathrm{background}})$. By construction, this discriminant is close to zero for backgroundlike events ($P_{\mathrm{background}} \gg P_{\mathrm{signal}}$) and close to unity for signal-like events ($P_{\mathrm{signal}} \gg P_{\mathrm{background}}$). Expressions (13) and (14) are the definitions of the event probability discriminants used in this analysis for single and double b-tagged events, respectively:

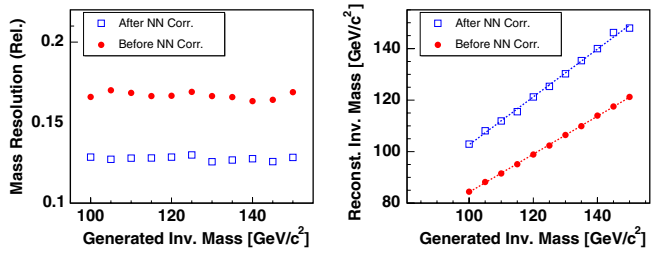

FIG. 19 (color online). Left (right) panel: Relative resolution, sigma divided by the mean of the Gaussian fit to the invariant mass distributions, as a function of the invariant mass (reconstructed vs generated invariant mass) before and after applying the NN correction to the measured jets.

$$\mathrm{EPD} \equiv \frac{b\hat{P}_{WH}}{b(\hat{P}_{WH} + \hat{P}_{Wb\bar{b}} + \hat{P}_{t\bar{t}} + \hat{P}_s + \hat{P}_t) + (1-b)(\hat{P}_{Wc\bar{c}} + \hat{P}_{Wcj} + \hat{P}_{W+l} + \hat{P}_{Wgg} + \hat{P}_{dib})}, \tag{13}$$

$$\mathrm{EPD} \equiv \frac{b_1 b_2 \hat{P}_{WH}}{b_1 b_2(\hat{P}_{WH} + \hat{P}_{Wb\bar{b}} + \hat{P}_{t\bar{t}} + \hat{P}_s) + b_1(1-b_2)\hat{P}_t + (1-b_1)(1-b_2)(\hat{P}_{Wc\bar{c}} + \hat{P}_{Wcj} + \hat{P}_{W+l} + \hat{P}_{Wgg} + \hat{P}_{dib})}, \tag{14}$$

where $\hat{P}_i = C_i \cdot P_i$, P_i is the event probability of a given physics process (WH, s channel, $Wb\bar{b}, \ldots$), C_i are additional coefficients (to be defined below), and b (defined as the b-jet probability) is a transformation of the output of the neural network jet flavor separator (b_{NN}) [37,57].

Extra nonkinematic information is introduced into the event probability discriminant by using b_{NN}, and C_i. The C_i coefficients are included into the EPD and used to optimize the discrimination power between signal and background. This set of coefficients is obtained by an iterative technique that involves the repeated generation of different sets of parameters and the computation of the expected limit for each set. However, because the calculation of limits with the inclusion of systematic uncertainties is computationally intensive, the optimization is implemented by performing a faster calculation for a figure of merit based only on statistical uncertainties. This has been successfully used in previous versions of this analysis and in the most recent measurement of the $WW + WZ$ production cross section [17].

For any given set of coefficients C_i, the Monte Carlo templates of the EPD variable are generated normalized to the corresponding number of expected signal and background events calculated in Sec. VII. The figure of merit is obtained from these templates using a maximum likelihood fit to extract ξ and its error σ_ξ, where ξ is a multiplicative factor to the expected WH cross section. The negative logarithm of the likelihood used is

$$-\log(\mathcal{L}(\xi)) = \sqrt{\sum_{k=1}^{n_{\mathrm{bin}}} \frac{(\xi S_k)^2}{\xi S_k + B_k + (\xi \Delta S_k)^2 + (\Delta B_k)^2}}, \tag{15}$$

where S_k and B_k are the expected number of signal and background events in the kth bin and ΔS_k and ΔB_k are the statistical uncertainty on S_k and B_k, respectively. The variable ξ represents the most likely value of signal, in units of the expected signal cross section, that can be fitted on the background templates and should be always close to zero after the minimization. The error on the value of ξ is obtained from the minimization and is related to the strength by which the signal can be differentiated from the background templates in units of the expected signal cross section; the larger the error the smaller the strength and vice versa. For each set of EPD templates the figure of merit is defined as $1/\sigma_\xi$.

The best set of coefficients is then obtained using an iterative technique, where at the beginning the current best set of coefficients is initially set to the maximum matrix element probability values obtained in the respective samples. For every iteration a trial set of coefficients is formed by introducing random changes in some of the coefficients from the current best set, creating new EPD templates and calculating the corresponding figure of merit of these new EPDs. The set of coefficients that produces the best figure of merit based on ~2000 iterations is considered optimal and used for the analysis.

After the event selection and applying b tagging, several of the sizable background processes do not have a b quark in the final state, but are falsely identified as such. This happens either because a light quark jet is falsely identified to have a displaced secondary vertex from the primary vertex due to tracking resolution (mistag) or because charm quark decays happen to have a sufficiently long lifetime to be tagged. Therefore, it would be desirable to have better separation of b-quark jets from charm or light quark jets. The neural network jet flavor separator is used to achieve this separation. As mentioned before, the b variable used in the EPD is a transformation of the b_{NN} in such a way that it goes from 0 to 1. The neural network jet flavor separator is a continuous variable and the result of a neural network training that uses a broad range of variables in order to identify b-quark jets with high purity [57]. A variety of variables is suitable to exploit the lifetime, mass, and decay multiplicity of b hadrons. Many of them are related to the reconstructed secondary vertex; some are reflected by the properties of the tracks in the SECVTX tagged jet. Including this factor helps to discriminate signal from background events and improves the final sensitivity.

The event probability discriminants are defined for all the MC events that pass the analysis selection (see Sec. IV) including events with at least one jet tagged by SECVTX. This provides sufficient MC statistics except for $W + LF$ and non-W events, so in these cases events with no tagged jets are also included.

The EPDs, for MC events, are defined independently of the tagging category of the event, but later on, when making the final templates, the events are weighted by the corresponding tagging probability. These tagging probabilities are the b-tagging correction factor ($\varepsilon_{\mathrm{tag}}$) used in Eqs. (3) and (4). They are functions of the flavor of the quark, the tagging scale factor and the mistag matrix, a parametrization of the mistag rate. If a jet is matched to a

heavy-flavor hadron [ΔR (jet, HF hadron) <0.4] and tagged by one of the b-tagging algorithms, the weight is the corresponding tagging scale factor (shown in Table II). If it is matched to a heavy-flavor hadron but the jet is not tagged by any of the b-tagging algorithms, the weight is set to zero. If the jet is not matched to heavy flavor, it is assigned a weight equal to its mistag probability (Sec. V C), regardless of whether or not it was tagged, because the Monte Carlo simulation does not properly model mistagging. On the other hand, for observed events, tagging is required and the events are not weighted by any tagging probability.

Since the neural network jet flavor separator b_{NN} is defined only for SECVTX tagged jets, it requires a special treatment for the events where any of the jets is not tagged. b_{NN} is used for each type of event; in the cases where the jet is not tagged the value of the b_{NN} is randomized using the light or non-W flavor separator template.

In the case of three-jet events (for two-jet events the same idea applies), for Eq. (13) (EPD for the SVJP and SVnoJP categories) the criteria for choosing b are as follows:

(i) if the three jets are SECVTX tagged, the b-jet probability of one of them is chosen randomly;
(ii) if two jets are SECVTX tagged, the b-jet probability of one of them is chosen randomly;
(iii) if one jet is SECVTX tagged, the b-jet probability of that jet is used;
(iv) if no jet is SECVTX tagged, the b-jet probability is randomized (a random value is taken from the light-flavor template for W + light events and from the non-W template for non-W events) for each of the 3 jets and one of them is chosen randomly.

For Eq. (14) (EPD for the SVSV category), the criteria for choosing b_1 and b_2 are as follows:

(i) if the three jets are SECVTX tagged, the b-jet probabilities of two of them are chosen randomly;
(ii) if two jets are SECVTX tagged, the b-jet probability of both of them is used (in random order);
(iii) if one jet is SECVTX tagged, the b-jet probability of the tagged jet and a random value out of the other jets are used (in random order);
(iv) if no jet is SECVTX tagged, the b-jet probability of the three jets is randomized and two of them are randomly chosen.

In the search for SM Higgs boson production, 12 separate EPD discriminants are created for each Higgs boson mass point, given by the different b-tagging categories (SVnoJP, SVJP, SVSV), the number of jets in the final state (2 and 3 jets), and the type of leptons (tight and EMC leptons). This gives the ability to tune the discriminants independently. Figures 20 and 21 show the signal and background templates, scaled to unit area, for two- and three-jet events, respectively, for each signal region. Note that in these figures all of the lepton categories have been combined.

D. Validation of the discriminant output

The performance of the Monte Carlo to predict the distribution of each EPD is validated by checking the untagged W + jet control samples, setting $b_{\mathrm{NN}} = 0.5$ so that it does not affect the EPD. An example is shown in Fig. 22 for W + 2-jet and W + 3-jet events. The agreement in this control sample gives confidence that the information used in this analysis is well modeled by the Monte Carlo simulation.

The ME method used here is further validated through its successful use in previous analyses at the CDF experiment to observe small signals with large backgrounds in similar final states to the one used here for the Higgs boson search. The method was used in the untagged W + jet sample to measure the cross section of diboson production [17]. In addition, it was used successfully in the tagged sample to measure the single top production cross section [37]. In the latter, the modeling was also checked for the discriminant output for a second control region—events with four jets. In this sample, dominated by top pair production, the EPD was also found to be well modeled [54].

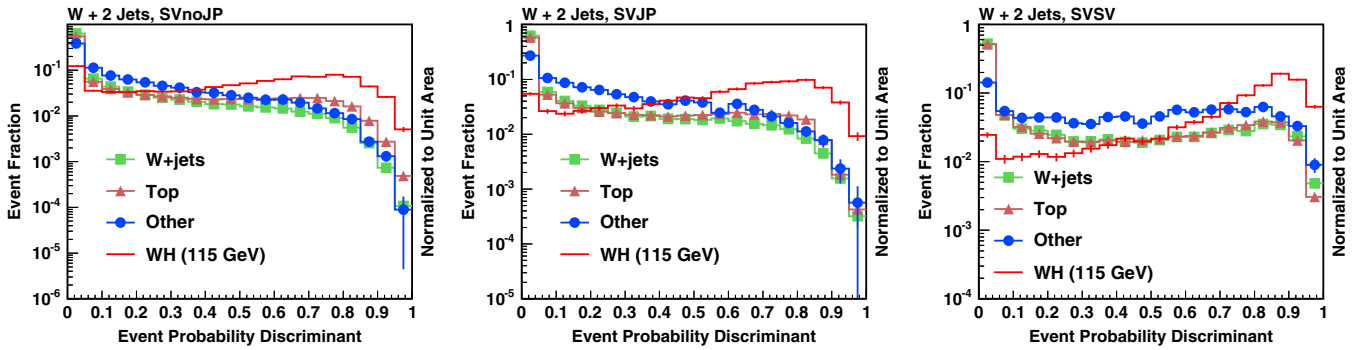

FIG. 20 (color online). Templates of predictions for the signal ($m_H = 115$ GeV/c^2) and background processes, each scaled to unit area, of the ME discriminant, EPD, for 2-jet events for each signal region.

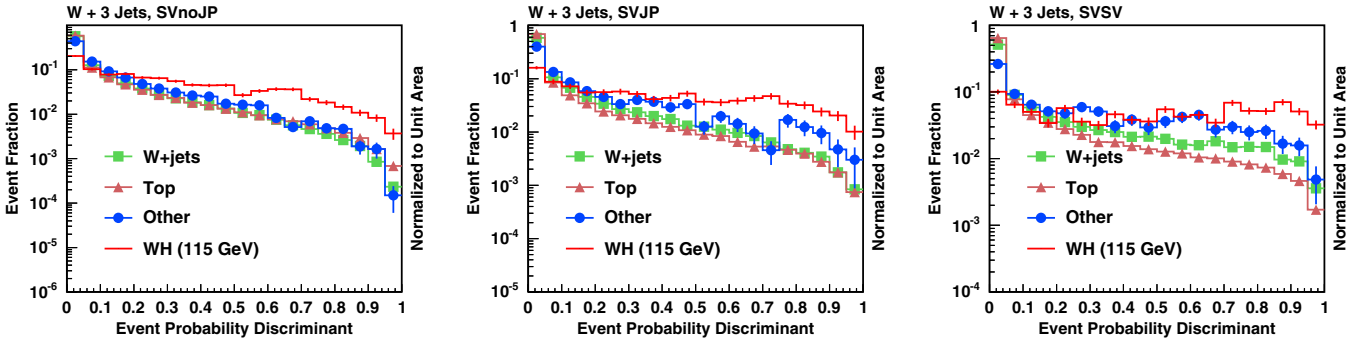

FIG. 21 (color online). Templates of predictions for the signal ($m_H = 115$ GeV/c^2) and background processes, each scaled to unit area, of the ME discriminant, EPD, for 3-jet events for each signal region.

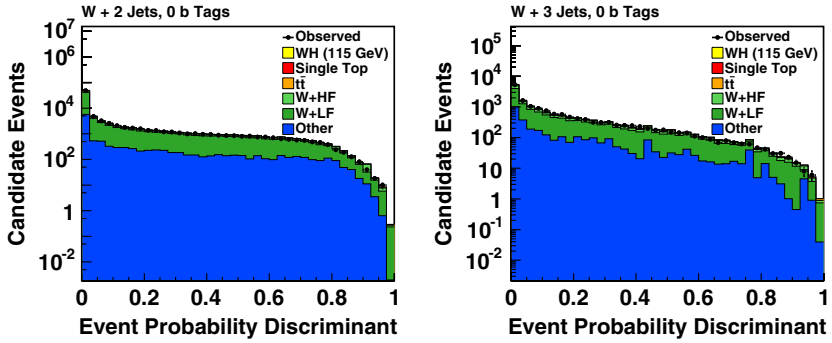

FIG. 22 (color online). Left (right) panel: The discriminant output for untagged $W + 2$ (3) jets control sample show that the Monte Carlo $W + 2$ (3) jets samples model the ME distribution of the observed events well.

IX. SYSTEMATIC UNCERTAINTIES

Systematic uncertainties can bias the outcome of this analysis and have to be incorporated into the result. The dominant systematic uncertainties addressed are from several different sources: jet-energy scale (JES), initial state radiation (ISR), final state radiation (FSR), parton distribution functions, lepton identification, luminosity, and b-tagging scale factors.

Systematic uncertainties can influence both the expected event yield (normalization) and the shape of the discriminant distribution. The dominant rate uncertainties have been included for each category. Shape uncertainties have only been applied for the JES, which has a small impact on the final sensitivity. Other shape uncertainties are expected to be small. When the sensitivity to signal events gets closer to the SM prediction the result will be

TABLE IX. Normalization systematic uncertainties on the signal and background contributions for the 2-jets channel. Some uncertainties are listed as ranges, as the impacts of the uncertain parameters depend on the tagging category. Systematic uncertainties for WH shown in this table are obtained for $m_H = 115$ GeV/c^2.

	Relative uncertainties (%)					
Contribution	W + HF	Mistags	Top	Diboson	Non-W	WH
Luminosity ($\sigma_{\text{inel}}(p\bar{p})$)			3.8	3.8		3.8
Luminosity monitor			4.4	4.4		4.4
Lepton ID			2	2		2
Jet-energy scale						2
ISR + FSR + PDF						3.1–5.6
b-tag efficiency			3.5–8.4	3.5–8.4		3.5–8.4
Cross section			10	10		10
HF fraction in W + jets	30					
Mistag rate		9–13.3				
Non-W rate					40	

TABLE X. Normalization systematic uncertainties on the signal and background contributions for the 3-jets channel. Some uncertainties are listed as ranges, as the impacts of the uncertain parameters depend on the tagging category. Systematic uncertainties for WH shown in this table are obtained for $m_H = 115$ GeV/c^2.

	Relative uncertainties (%)					
Contribution	W + HF	Mistags	Top	Diboson	Non-W	WH
Luminosity ($\sigma_{\text{inel}}(p\bar{p})$)			3.8	3.8		3.8
Luminosity monitor			4.4	4.4		4.4
Lepton ID			2	2		2
Jet-energy scale						13.5–15.8
ISR + FSR + PDF						13.1–21.4
b-tag efficiency			3.5–8.4	3.5–8.4		3.5–8.4
Cross section			10	10		10
HF fraction in W + jets	30					
Mistag rate		9–13.3				
Non-W rate					40	

more affected by sources of systematic uncertainties; currently, this analysis is statistically limited.

Normalization uncertainties are estimated by recalculating the acceptance using Monte Carlo samples altered due to a specific systematic effect. The normalization uncertainty is the difference between the systematically shifted acceptance and the default one. The normalization uncertainties for signal and background processes are shown in Tables IX (for two-jet events) and X (for three-jet events).[2]

The effect of the uncertainty in the jet-energy scale is evaluated by applying jet-energy corrections that describe $\pm 1\sigma$ variations to the default correction factor. The JES shape uncertainty has been only applied to the event probability discriminant for the two- and three-jet events in the samples with the biggest contribution, for the WH signal sample, and the W + jets and $t\bar{t}$ background samples. Shape variations due to the jet-energy scale for two- and three-jet WH signal events are shown in Fig. 23. The effect of the JES shape uncertainty on the final sensitivity is small, on the order of only a few percent. This is small compared to the effect of normalization uncertainties.

Systematic uncertainties due to the modeling of ISR and FSR are obtained from dedicated Monte Carlo samples for WH signal events where the strength of ISR/FSR is increased and decreased in the parton showering to represent $\pm 1\sigma$ variations [58]. The effects of variations in ISR and FSR are treated as 100% correlated with each other.

To evaluate the uncertainty on the signal acceptance associated with the specific choice of parton distribution functions, events are reweighted based on different PDF schemes. The 20 independent eigenvectors of the CTEQ [42] PDFs are varied and compared to the MRST [59]

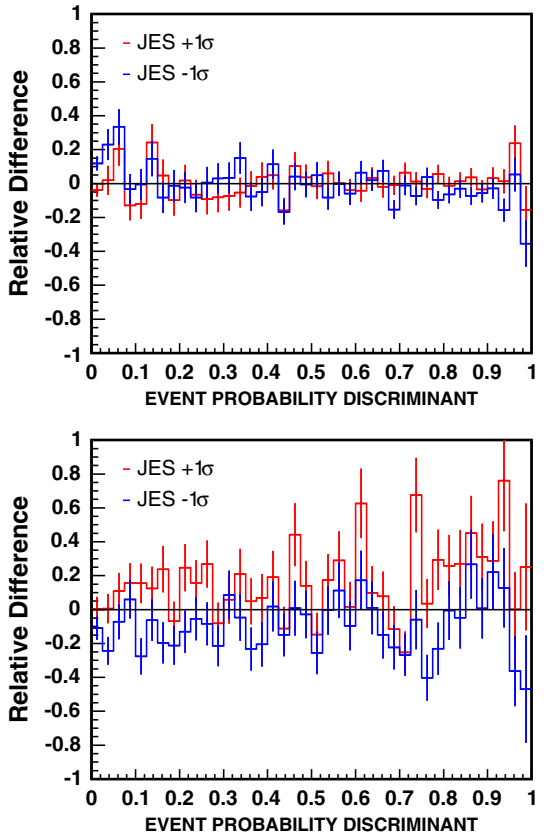

FIG. 23 (color online). Top (bottom) panel: WH ($m_H = 115$ GeV/c^2) JES shape systematic for two- (three-) jet events. The plots show the relative difference of one σ up and one σ down jet-energy correction with respect to the nominal correction.

[2]Note that empty entries in the table either mean that the systematic is not relevant for that process (for example, background rates that are derived from data are not affected by the uncertainty on the luminosity measurement), or that it was studied and found to be negligible (for example, effect of the JES uncertainty was studied for dibosons and top production and found to have a negligible impact on the final sensitivity).

PDFs. The uncertainty from the CTEQ and MRST PDF uncertainty are summed in quadrature if the difference between the CTEQ and MRST PDFs is larger than the CTEQ uncertainty.

The estimate of the lepton ID uncertainty is a result of varying the lepton ID correction factors. The results are then compared to the nominal prediction for an estimate of the fractional uncertainty. All lepton ID correction factors are varied either all up or all down simultaneously. The yield is then calculated for each sample and compared to the nominal prediction. The lepton ID uncertainty is applied to the signal sample and all Monte Carlo based samples.

For the signal sample and all Monte Carlo based samples a systematic uncertainty is applied for the uncertainty in the CDF luminosity measurement which is correlated across all samples and channels. This uncertainty includes the uncertainty in the $p\bar{p}$ inelastic cross section (3.8%) as well as the uncertainty in the acceptance of CDF's luminosity monitor (4.4%) [60].

The effect of the b-tagging scale factor uncertainty is determined from the background estimate. The systematic uncertainty on the event tagging efficiency is estimated by varying the tagging scale factor and mistag prediction by $\pm 1\sigma$ and calculating the difference between the systematically shifted acceptance and the default one.

For all background processes the normalization uncertainties are represented by the uncertainty on the predicted number of background events and are incorporated in the analysis as Gaussian constraints $G(\beta_j|1, \Delta_j)$ in a likelihood function [37]. The systematic uncertainties in the normalizations of each source, β_j, are incorporated into the likelihood as nuisance parameters, conforming with a fully Bayesian treatment [61]. The correlations between normalizations for a given source are taken into account. The likelihood function is marginalized by integrating over all nuisance parameters for many possible values of the WH cross section $\beta_1 = \beta_{WH}$. The resulting reduced likelihood $\mathcal{L}(\beta_{WH})$ is a function of the WH cross section β_{WH} only. More details on the statistical treatment of the limit calculation are included in Refs. [37,52].

X. RESULTS

The analysis is applied to observed events in a sample corresponding to an integrated luminosity of 5.6 fb^{-1}. The EPD output distribution, for a Higgs boson mass of 115 GeV/c^2, of our candidate events is compared with the sum of predicted WH signal and background distributions as shown in Fig. 24.

We search for an excess of Higgs boson signal events in the EPD distributions, but no evidence of a signal excess is

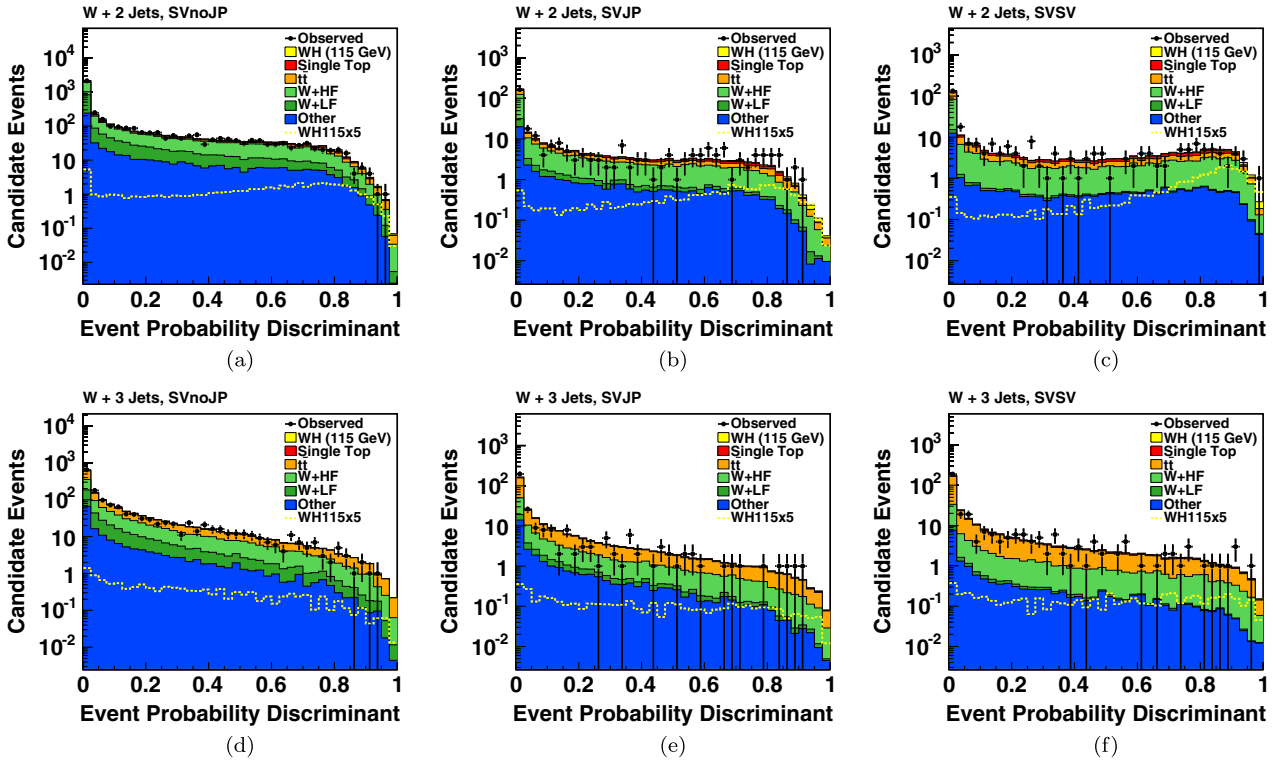

FIG. 24 (color online). Top (a)–(c) [bottom (d)–(f)]: Comparison of the EPD output for lepton + 2 (3) jets observed events compared to the Monte Carlo simulated events for WH ($m_H = 115$ GeV/c^2) signal and background. From left to right: SVnoJP, SVJP, and SVSV tagged observed events, respectively. Note that the signal is twice in these plots, as a stacked plot and as a histogram multiplied by 5 ($\times 5$).

TABLE XI. Expected and observed upper limit cross sections, relative to the SM prediction, for different Higgs boson mass points for 2- and 3-jet events.

	2, 3 jets										
σ/SM	100	105	110	115	120	125	130	135	140	145	150
Expected	2.5	2.7	3.0	3.5	4.4	5.1	6.6	8.7	13.0	17.8	27.5
Observed	2.1	2.6	3.2	3.6	4.6	5.3	8.3	9.2	14.8	18.9	35.3

found in the observed events. Thus, we perform a binned likelihood fit to the EPD output distributions to set an upper limit on SM Higgs boson production associated with a W boson for 11 values of m_H, $100 \leq m_H \leq 150$ GeV/c^2 in 5 GeV/c^2 steps.

In order to extract the most probable WH signal content in the observed events the maximum likelihood method described before is performed. A marginalization using the likelihood function is performed with all systematic uncertainties included in the likelihood function. The posterior PDF is obtained by using Bayes' theorem:

$$p(\beta_1|\mathrm{EPD}) = \frac{\mathcal{L}^*(\mathrm{EPD}|\beta_{WH})\pi(\beta_{WH})}{\int \mathcal{L}^*(\mathrm{EPD}|\beta'_{WH})\pi(\beta'_{WH})d\beta'_{WH}},$$

where $\mathcal{L}^*(\mathrm{EPD}|\beta_{WH})$ is the reduced likelihood and $\pi(\beta_{WH})$ is the prior PDF for β_{WH}. A flat prior is adopted, $\pi(\beta_{WH}) = H(\beta_{WH})$, in this analysis, with H being the Heaviside step function. To set an upper limit on the WH production cross section, the posterior probability density is integrated to cover 95% [52].

The observed and expected limits on $\sigma(p\bar{p} \to WH) \times \mathcal{B}(H \to b\bar{b})$, for each Higgs boson mass point from 100 to 150 GeV/c^2 in 5 GeV/c^2 steps, all b-tagging categories, and 2- and 3-jet events together are shown in Table XI and

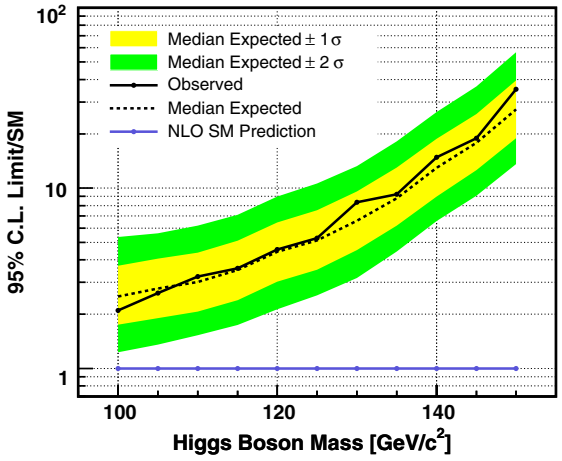

FIG. 25 (color online). 95% C.L. upper limits on the WH production cross sections times branching ratio for $H \to b\bar{b}$ for Higgs boson masses between $m_H = 100$ GeV/c^2 to $m_H = 150$ GeV/c^2. The plot shows the limit normalized to the cross section predictions from the standard model.

TABLE XII. Expected and observed upper limit on $\sigma(p\bar{p} \to WH) \times \mathcal{B}(H \to b\bar{b})$ in units of pb for different Higgs boson mass points for 2- and 3-jet events.

	2, 3 jets										
σ	100	105	110	115	120	125	130	135	140	145	150
Exp	0.72	0.68	0.66	0.65	0.67	0.69	0.79	0.90	1.12	1.39	1.93
Obs	0.60	0.66	0.70	0.67	0.70	0.72	1.00	0.95	1.27	1.47	2.47

TABLE XIII. Expected and observed upper limit cross sections, relative to the SM prediction, for different Higgs boson mass points in the 2-jets channel.

	2 jets										
σ/SM	100	105	110	115	120	125	130	135	140	145	150
Expected	2.6	2.8	3.2	3.7	4.7	5.5	7.1	9.5	14.2	19.7	30.7
Observed	2.7	3.3	3.7	4.5	5.9	6.8	9.6	12.0	19.3	24.0	43.2

TABLE XIV. Expected and observed upper limit cross sections, relative to the SM prediction, for different Higgs boson mass points in the 3-jets channel.

	3 jets										
σ/SM	100	105	110	115	120	125	130	135	140	145	150
Expected	12.2	12.9	13.9	15.8	19.5	23.0	28.1	39.5	56.1	77.9	120
Observed	5.1	5.6	8.6	8.5	10.8	12.4	17.3	22.9	33.7	42.5	81

in Fig. 25. The observed and expected limits in SM cross section units are shown in Table XII.

Tables XIII and XIV show the expected and observed limits, for each Higgs boson mass point, for events with 2 and 3 jets, respectively. Including 3-jet events improves the limit by 3% to 10%, depending on the Higgs boson mass, with respect to the result using 2-jet events only.

XI. CONCLUSIONS

A search for the Higgs boson production in association with a W boson using a matrix element technique has been performed using 5.6 fb^{-1} of CDF data. A maximum likelihood technique has been applied to extract the most probable WH content in observed events. No evidence is observed for a Higgs boson signal using observed events corresponding to an integrated luminosity of 5.6 fb^{-1} and 95% confidence level upper limits are set. The limits on the WH production cross section times the branching ratio, relative to the SM prediction, of the Higgs boson to decay to $b\bar{b}$ pairs are $\sigma(p\bar{p} \to WH) \times \mathcal{B}(H \to b\bar{b})/SM < 2.1$ to 35.3 for Higgs boson masses between $m_H = 100$ GeV/c^2 and $m_H = 150$ GeV/c^2. The expected (median) sensitivity estimated in pseudoexperiments is $\sigma(p\bar{p} \to WH) \times \mathcal{B}(H \to b\bar{b})/SM < 2.5$ to 27.5 at 95% C.L.

The search results in this channel at the CDF experiment are the most sensitive low-mass Higgs boson search at the Tevatron. While the LHC experiments will soon have superior sensitivity to the low-mass Higgs boson, this sensitivity comes primarily from searches in the diphoton final state. Therefore, we expect that the searches in the $H \rightarrow b\bar{b}$ at the Tevatron will provide crucial information on the existence and nature of the low-mass Higgs boson for years to come.

ACKNOWLEDGMENTS

We thank the Fermilab staff and the technical staffs of the participating institutions for their vital contributions. This work was supported by the U.S. Department of Energy and National Science Foundation; the Italian Istituto Nazionale di Fisica Nucleare; the Ministry of Education, Culture, Sports, Science and Technology of Japan; the Natural Sciences and Engineering Research Council of Canada; the National Science Council of the Republic of China; the Swiss National Science Foundation; the A. P. Sloan Foundation; the Bundesministerium für Bildung und Forschung, Germany; the Korean World Class University Program, the National Research Foundation of Korea; the Science and Technology Facilities Council and the Royal Society, UK; the Russian Foundation for Basic Research; the Ministerio de Ciencia e Innovación, and Programa Consolider-Ingenio 2010, Spain; the Slovak R&D Agency; the Academy of Finland; and the Australian Research Council (ARC).

[1] P. Higgs, Phys. Rev. Lett. **13**, 508 (1964).
[2] G. S. Guralnik, C. R. Hagen, and T. W. B. Kibble, Phys. Rev. Lett. **13**, 585 (1964).
[3] F. Englert and R. Brout, Phys. Rev. Lett. **13**, 321 (1964).
[4] R. Barate *et al.* (LEP Higgs Working Group), Phys. Lett. B **565**, 61 (2003).
[5] The Tevatron New Phenomena and Higgs Working Group, arXiv:1107.5518.
[6] LEP-Tevatron-SLD Electroweak Working Group, ALEPH, CDF, D0, DELPHI, L3, OPAL, and SLD Collaborations), arXiv:0911.2604.
[7] A. Djouadi, J. Kalinowski, and M. Spira, Comput. Phys. Commun. **108**, 56 (1998).
[8] T. Han and S. Willenbrock, Phys. Lett. B **273**, 167 (1991).
[9] S. Chatrchyan *et al.* (CMS Collaboration), Report No. CMS-PAS-HIG-11-022.
[10] G. Aad *et al.* (ATLAS Collaboration), Phys. Lett. B **705**, 452 (2011).
[11] S. Chatrchyan *et al.* (CMS Collaboration), Report No. CMS-PAS-HIG-11-012.
[12] T. Aaltonen *et al.* (CDF Collaboration), Phys. Rev. Lett. **103**, 101802 (2009).
[13] V. M. Abazov *et al.* (D0 Collaboration), Phys. Lett. B **698**, 6 (2011).
[14] M. F. Canelli, Ph.D. thesis, University of Rochester [Report No. FERMILAB-THESIS-2003-22, 2003].
[15] B. N. Mohr, Ph.D. thesis, University of California Los Angeles [Report No. FERMILAB-THESIS-2007-05, 2007].
[16] T. Aaltonen *et al.* (CDF Collaboration), Phys. Rev. Lett. **103**, 092002 (2009).
[17] T. Aaltonen *et al.* (CDF Collaboration), Phys. Rev. D **82**, 112001 (2010).
[18] T. Aaltonen *et al.* (CDF Collaboration), Phys. Rev. Lett. **99**, 182002 (2007).
[19] T. Aaltonen *et al.* (CDF Collaboration), Phys. Rev. Lett. **104**, 061803 (2010).
[20] T. Aaltonen *et al.* (CDF Collaboration), Phys. Rev. Lett. **104**, 201801 (2010).
[21] R. Blair *et al.* (CDF Collaboration), Report No. FERMILAB-PUB-96/390-E, 1996.
[22] D. Acosta *et al.* (CDF Collaboration), Phys. Rev. D **71**, 032001 (2005).
[23] C. S. Hill (CDF Collaboration), Nucl. Instrum. Methods Phys. Res., Sect. A **530**, 1 (2004).
[24] A. Sill (CDF Collaboration), Nucl. Instrum. Methods Phys. Res., Sect. A **447**, 1 (2000).
[25] A. A. Affolder *et al.* (CDF Collaboration), Nucl. Instrum. Methods Phys. Res., Sect. A **453**, 84 (2000).
[26] A. A. Affolder *et al.* (CDF Collaboration), Nucl. Instrum. Methods Phys. Res., Sect. A **526**, 249 (2004).
[27] L. Balka *et al.* (CDF Collaboration), Nucl. Instrum. Methods Phys. Res., Sect. A **267**, 272 (1988).
[28] S. Bertolucci *et al.* (CDF Collaboration), Nucl. Instrum. Methods Phys. Res., Sect. A **267**, 301 (1988).
[29] M. G. Albrow *et al.* (CDF Collaboration), Nucl. Instrum. Methods Phys. Res., Sect. A **480**, 524 (2002).
[30] G. Ascoli, L. E. Holloway, I. Karliner, U. E. Kruse, R. D. Sard, V. J. Simaitis, D. A. Smith, and T. K. Westhusing, Nucl. Instrum. Methods Phys. Res., Sect. A **268**, 33 (1988).
[31] T. Dorigo *et al.* (CDF Collaboration), Nucl. Instrum. Methods Phys. Res., Sect. A **461**, 560 (2001).
[32] E. J. Thomson, C. Ciobanu, J. Chung, J. Gerstenslager, J. Hoftiezer *et al.*, IEEE Trans. Nucl. Sci. **49**, 1063 (2002).
[33] R. Downing, N. Eddy, L. Holloway, M. Kasten, H. Kim, J. Kraus, C. Marino, K. Pitts, J. Strologas, and A. Taffard, Nucl. Instrum. Methods Phys. Res., Sect. A **570**, 36 (2007).
[34] G. Gomez-Ceballos, A. Belloni, A. Bolshov, B. Iyutin, I. Kravchenko, N. Leonardo, B. Knuteson, Ch. Paus, S. Tether, J. Tseng, and F. Wurthwein, Nucl. Instrum. Methods Phys. Res., Sect. A **518**, 522 (2004).
[35] B. Casal, Ph.D. thesis, University of Cantabria [Report No. FERMILAB-THESIS-2009-21, 2009].

[36] A. Bhatti *et al.*, Nucl. Instrum. Methods Phys. Res., Sect. A **566**, 375 (2006).
[37] T. Aaltonen *et al.* (CDF Collaboration), Phys. Rev. D **82**, 112005 (2010).
[38] D. E. Acosta *et al.* (CDF Collaboration), Phys. Rev. D **71**, 052003 (2005).
[39] A. Abulencia *et al.* (CDF Collaboration), Phys. Rev. D **74**, 072006 (2006).
[40] C. Neu, Report No. FERMILAB-CONF-06-162-E, 2006.
[41] T. Sjöstrand, P. Edén, C. Friberg, L. Lönnblad, G. Miu, S. Mrenna, and E. Norrbin, Comput. Phys. Commun. **135**, 238 (2001).
[42] H. L. Lai *et al.* (CTEQ Collaboration), Eur. Phys. J. C **12**, 375 (2000).
[43] R. Brun and F. Carminati, W5013 (1993).
[44] T. Aaltonen *et al.* (CDF Collaboration), Phys. Rev. D **82**, 034001 (2010).
[45] T. H. W. Group, arXiv:hep-ph/0406152.
[46] F. Maltoni and T. Stelzer, J. High Energy Phys. 02 (2003) 027.
[47] M. L. Mangano, M. Moretti, F. Piccinini, R. Pittau, and A. D. Polosa, J. High Energy Phys. 07 (2003) 001.
[48] J. M. Campbell and R. K. Ellis, Phys. Rev. D **60**, 113006 (1999).
[49] T. Aaltonen *et al.* (CDF Collaboration), Phys. Rev. Lett. **100**, 102001 (2008).
[50] M. Cacciari, S. Frixione, M. L. Mangano, P. Nason, and G. Ridolfi, J. High Energy Phys. 09 (2008) 127.
[51] B. Harris, E. Laenen, L. Phaf, Z. Sullivan, and S. Weinzierl, Phys. Rev. D **66**, 054024 (2002).
[52] K. Nakamura *et al.* (Particle Data Group), J. Phys. G **37**, 075021 (2010).
[53] I. Murayama, H. Watanabe, and K. Hagiwara, KEK Technical Report No. 91-11, 1992.
[54] P. J. Dong, Ph.D. thesis, University of California Los Angeles [Report No. FERMILAB-THESIS-2008-12, 2008].
[55] SNNS is (c) (Copyright) 1990-95 SNNS Group, Institute for Parallel and Distributed High-Performance Systems (IPVR), University of Stuttgart, Breitwiesenstrasse 20-22, 70565 Stuttgart, Federal Republic of Germany [http://www.ra.cs.uni-tuebingen.de/SNNS/].
[56] B. Alvarez, Ph.D. thesis, University of Cantabria [Report No. FERMILAB-THESIS-2010-25, 2010].
[57] S. Richter, Ph.D. thesis, University of Karlsruhe [Report No. FERMILAB-THESIS-2007-35, 2007].
[58] A. Abulencia *et al.* (CDF Collaboration), Phys. Rev. D **73**, 032003 (2006).
[59] A. D. Martin, R. G. Roberts, W. J. Stirling, and R. S. Thorne, Eur. Phys. J. C **4**, 463 (1998).
[60] D. Acosta *et al.*, Nucl. Instrum. Methods Phys. Res., Sect. A **494**, 57 (2002).
[61] L. Demortier, *Proceedings of Advanced Statistical Techniques in Particle Physics* (Grey College, Durham, 2002).